

Phase Functions and Light Curves of Wide Separation Extrasolar Giant PlanetsDavid Sudarsky¹, Adam Burrows¹, Ivan Hubeny¹, & Aigen Li^{1,2}**ABSTRACT**

We calculate self-consistent extrasolar giant planet (EGP) phase functions and light curves for orbital distances ranging from 0.2 AU to 15 AU. We explore the dependence on wavelength, cloud condensation, and Keplerian orbital elements. We find that the light curves of EGPs depend strongly on wavelength, the presence of clouds, and cloud particle sizes. Furthermore, the optical and infrared colors of most EGPs are phase-dependent, tending to be reddest at crescent phases in $V - R$ and $R - I$. Assuming circular orbits, we find that at optical wavelengths most EGPs are 3 to 4 times brighter near full phase than near greatest elongation for highly inclined (i.e., close to edge-on) orbits. Furthermore, we show that the planet/star flux ratios depend strongly on the Keplerian elements of the orbit, particularly inclination and eccentricity. Given a sufficiently eccentric orbit, an EGP's atmosphere may make periodic transitions from cloudy to cloud-free, an effect that may be reflected in the shape and magnitude of the planet's light curve. Such elliptical orbits also introduce an offset between the time of the planet's light curve maximum and the time of full planetary phase, and for some sets of orbital parameters, this light curve maximum can be a steeply increasing function of eccentricity. We investigate the detectability of EGPs by proposed space-based direct-imaging instruments.

Subject headings: planetary systems—binaries: general—planets and satellites: general—radiative transfer

1. Introduction

Over the past several years, a wide variety of nearby extrasolar giant planet (EGP) systems has been detected indirectly by radial velocity techniques (e.g., Mayor & Queloz 1995; Marcy & Butler 1996; Marcy *et al.* 1998, 1999, 2002; Butler *et al.* 1997, 1999, 2002; Queloz *et al.* 2000). Model atmospheres and spectra for a fraction of these objects have been developed (Seager & Sasselov 1998; Barman *et al.* 2001; Sudarsky, Burrows, & Hubeny 2003; Burrows, Sudarsky, & Hubeny 2004)

¹Department of Astronomy and Steward Observatory, The University of Arizona, Tucson, AZ 85721

²Lunar and Planetary Laboratory, The University of Arizona, Tucson, AZ 85721

to guide ground- and space-based observations. However, most studies to date have not addressed the dependence of EGP spectra and colors on planetary phase, which, along with ephemerides, may be crucial to the interpretation of directly imaged EGPs.

Some attention has been given to the self-consistent modeling of planetary phase functions and light curves for the close-in EGPs ($\lesssim 0.05$ AU; Seager *et al.* 2000; Green *et al.* 2003), but at wider separations, simple Lambert reflection models (isotropic surface reflection; Sobolev 1975) or fits to reflection data for the giant planets of our solar system have been utilized. While much of their recent paper focuses on ringed extrasolar planets, Arnold & Schneider (2004) study the phase dependence of a ringless planet as a function of orbital inclination by assuming Lambert reflection. The spectral dependence of the light curves is not investigated, and a geometric albedo is assumed, rather than computed. Dyudina *et al.* (2004) model the light curves of ringed and ringless EGPs by using red-band *Pioneer* phase data for Jupiter and Saturn. A functional fit to these data allows them to construct planetary phase functions, from new to full phase. EGP light curves for various distances and eccentricities are then derived, assuming these planetary phase curves. Due to the limitations of the *Pioneer* data, they could not investigate the dependence on wavelength or cloud condensates and particle sizes. Furthermore, they could not explore the dependence of the albedos and phase functions on orbital distance.

With numerous space-based instruments under development that will be capable of detecting EGPs in the optical or near infrared spectral regions (e.g. *Eclipse*, Trauger *et al.* 2000, 2001; *EPIC*, Clampin *et al.* 2002, Lyon *et al.* 2003; *Terrestrial Planet Finder*, Beichman *et al.* 2002; *Kepler*, Koch *et al.* 1998; *Corot*, Antonello & Ruiz 2002; *MONS*, Christensen-Dalsgaard 2000; *MOST*, Matthews *et al.* 2001), wavelength-dependent planetary phase models for a range of orbital distances will be in demand. In this work, we compute self-consistent, solar-metallicity atmosphere models of EGPs and derive albedos, phase integrals, phase functions, and light curves as a function of wavelength. The effects of varying the Keplerian elements, including semi-major axis, orbital inclination, eccentricity, argument of periastron, and longitude of the ascending node are investigated. Because atmospheric compositions vary enormously with orbital distance, a detailed and self-consistent approach is necessary. Our present model set spans orbital radii from 0.2 AU to 15 AU, thereby encompassing a great variety of atmospheric structures.

In §2, we review the formalism associated with our treatment of planetary phase functions and include a description of our numerical methods. Section 3 contains a sampling of Solar System phase functions, while §4 details our model phase functions for EGPs. Section 5 contains geometric and spherical albedo spectra for a full range of EGP orbital distances. Wavelength-dependent EGP light curves for circular orbits are presented in §6. Section 7 details the dependence of EGP colors on planetary phase. Section 8 investigates the effects of cloud particle size variation on EGP light curves. In §9, we explore the important effects of eccentricity and viewing angle on the resulting light curves. We conclude with a summary and discuss in §10 prospects for the detection of wide-separation EGPs and their light curves.

2. Formalism and Numerical Techniques

It is useful to review important definitions and quantities relevant to the study of planetary phases and light curves. Planetary phase is a function of the observer-planet-star orientation, and the angle whose vertex lies at the planet is known as the *phase angle* (α). The requisite formalism for the computation of planetary brightness as a function of phase angle has been presented by numerous authors. Following Sobolev (1975), we relate the planetary latitude (ψ) and longitude (ξ) to the cosine of the angle of incident radiation (μ_0) and the cosine of the angle of emergent radiation (μ) at each point on the planet’s surface:

$$\mu_0 = \cos \psi \cos(\alpha - \xi) \quad (1)$$

and

$$\mu = \cos \psi \cos \xi, \quad (2)$$

where latitude is measured from the orbital plane and longitude is measured from the observer’s line of sight. The phase angle is then,

$$\alpha = \cos^{-1} \left(\mu\mu_0 - [(1 - \mu^2)(1 - \mu_0^2)]^{1/2} \cos\phi \right), \quad (3)$$

where ϕ is the azimuthal angle between the incident and emergent radiation at a point on the planet’s surface. The emergent intensity from a given planetary latitude and longitude is given by

$$I(\mu, \mu_0, \phi) = \mu_0 S \rho(\mu, \mu_0, \phi), \quad (4)$$

where the incident flux on a small patch of the planet’s surface is $\pi\mu_0 S$, and $\rho(\mu, \mu_0, \phi)$ is the reflection coefficient. In order to compute the energy reflected off the entire planet, one must integrate over the surface of the planet. For a given planetary phase, the energy per second per unit area per unit solid angle received by an observer is

$$E(\alpha) = 2S \frac{R_p^2}{d^2} \int_{\alpha-\pi/2}^{\pi/2} \cos(\alpha - \xi) \cos(\xi) d\xi \int_0^{\pi/2} \rho(\mu, \mu_0, \phi) \cos^3 \psi d\psi, \quad (5)$$

where R_p is the planet’s radius and d is the distance to the observer. This quantity is related to the *geometric albedo* (A_g), the reflectivity of an object at full phase ($\alpha = 0$) relative to that of a perfect Lambert disk of the same radius under the same incident flux, by

$$A_g = \frac{E_p(0)d^2}{\pi S R^2}. \quad (6)$$

A planet in orbit about its central star displays a range of phases, and the planet/star flux ratio is given by

$$\frac{F_p}{F_*} = A_g \left(\frac{R_p}{a} \right)^2 \Phi(\alpha), \quad (7)$$

where $\Phi(\alpha)$ is the classical *phase function* ($= E(\alpha)/E(0)$), R_p is the planet’s radius, and a is its orbital distance. The planet/star flux ratio is the central formula of this paper, and the calculation of A_g and $\Phi(\alpha)$ is our major focus.

The *spherical albedo* is the fraction of incident light reflected by a sphere at all angles. For a theoretical object with absolutely no absorptive opacity, all incident radiation is scattered, resulting in a spherical albedo of unity. The spherical albedo is related to the geometric albedo by $A_s = qA_g$, where q is the *phase integral*:

$$q = 2 \int_0^\pi \Phi(\alpha) \sin \alpha d\alpha. \quad (8)$$

For isotropic surface reflection (Lambert reflection) $q = \frac{3}{2}$, while for pure Rayleigh scattering $q = \frac{4}{3}$. Although not written explicitly, all of the above quantities are functions of frequency (ν).

2.1. Keplerian Elements

In order to produce a model light curve for a planet orbiting its central star, one must relate the planet’s orbital angle (θ), as measured from periastron (periapse), to the time (t) in the planet’s orbit (Fig. 1):

$$t(\theta) = \frac{-(1 - e^2)^{1/2} P}{2\pi} \left(\frac{e \sin \theta}{1 + e \cos \theta} - 2(1 - e^2)^{-1/2} \tan^{-1} \left[\frac{(1 - e^2)^{1/2} \tan(\theta/2)}{1 + e} \right] \right), \quad (9)$$

where P is the orbital period and e is the eccentricity. Other important orbital elements include the orbital inclination (i), the longitude of the ascending node (Ω), and the argument of periastron (ω ; a.k.a. argument of periapse). The orbital inclination ranges from 0° for fully face-on orbits to 90° for edge-on orbits. The *ascending node* is the point in an orbit of the south-to-north crossing of the planet through the horizontal plane of the observer’s line of sight. Ω is the angle between the observer’s line of sight and the intersection of the observer’s plane and the orbital plane (the line of nodes). The argument of periastron is the angular distance measured along the orbit from the ascending node to periastron. For $\Omega = 90^\circ$, the line of nodes is perpendicular to the observer’s line of sight, and this is our default value. For an arbitrary orientation of an orbit, the phase angle is related to the above orbital elements by

$$\cos(\alpha) = \sin(\theta + \omega) \sin(i) \sin(\Omega) - \cos(\Omega) \cos(\theta + \omega). \quad (10)$$

By combining eq. (9) and (10), we derive the exact phase of any orbit at any time.

2.2. Atmosphere Code

We obtain each EGP atmospheric temperature-pressure (T-P) structure with our version of the *TLUSTY* 1-D atmosphere code (Hubeny & Lanz 1995), as described by Sudarsky, Burrows, & Hubeny (2003). In this process, the external radiation is assumed to be isotropic (i.e., it is averaged over all angles). For each resulting T-P structure, we employ a new 2-D version of *TLUSTY* (Hubeny 2005) in order to obtain the reflection coefficient, $\rho(\mu, \mu_0, \phi, \nu)$, at any latitude

and longitude on the planet’s “surface” (i.e., the atmosphere). We assume that the planet is spherical and take small areal patches on the surface that are essentially planar, but that are irradiated at different angles depending on their latitude and longitude. The local patches are assumed to be spatially 1-D (i.e., they are locally plane-parallel, horizontally-homogeneous layers). The radiative transfer is 2-D in angle, so that the anisotropic scattering phase function and (strongly) anisotropic irradiation are treated exactly. Details of the 2-D radiative transfer technique are given in Appendix A.

Figure 2 depicts a selection of our theoretical T-P profiles, along with the condensation curves for ammonia and water. Those model T-P profiles that cross the condensation curves contain clouds of the respective species. For example, in Fig. 2, the T-P profile for the 3 AU model intersects the H₂O condensation curve, but not the NH₃ curve. Therefore, this EGP contains a water cloud layer, but its ammonia remains in gaseous form. For each model, the frequency-integrated flux at the base of the atmosphere is set equal to the integrated emergent flux of a 1- M_J , 5-Gyr, non-irradiated EGP, which has an effective temperature of ~ 100 K. (Burrows *et al.* 1997). Although such a prescription is invalid for full evolutionary models of irradiated EGPs, this choice is perfectly acceptable for the present study; optical/near-infrared phase functions and light curves are not sensitive to this internal flux because it is low relative to the incident stellar flux.

With the resulting wavelength-dependent reflection coefficients, we integrate over the planetary surface to obtain the planetary phase function. With our numerical technique, we have reproduced the analytic Lambert phase function (Sobolev 1975) and the Lommel-Seeliger phase function (van de Hulst 1980) to better than 0.1%.

2.3. Atmospheric Composition

The realistic representation of condensate clouds is important in the production of accurate planetary model phase functions, because ices and grains are generally far more reflective and have much sharper angular phase dependences (single-particle phase functions) than gases. In this vein, we use a full Mie theory code (Li & Greenberg 1997), which computes accurate angular scattering phase functions up to size parameters of $2\pi a_0/\lambda \sim 6000$, where a_0 is the particle radius, and λ is the wavelength of light. Optical constants are taken from Martonchik *et al.* (1984; ammonia ice), and Warren (1984, 1991; H₂O ice).

We employ a cloud prescription that automatically positions the cloud base at the intersection of the atmospheric T-P profile and the condensate curve. The cloud position is updated with each iteration of the atmosphere code, so that the final converged model is derived in a self-consistent manner. A Deirmendjian (1964) particle size distribution is used, and the actual modal particle size is determined numerically using the prescription of Cooper *et al.* (2003). For simplicity, the vertical extent of each cloud layer is set to one pressure scale height, an approximation that is guided by the cloud model prescription used. Adaptive numerical zoning is used to resolve the cloud carefully

from top to bottom. Previous investigations selected particle sizes more arbitrarily and, in some cases, distributed these particles homogeneously throughout the atmosphere (i.e., created clouds with infinite scale heights).

Gaseous opacities include those from the set of atomic and molecular species described in Burrows *et al.* (2001) and Sudarsky, Burrows, & Hubeny (2003). We use the rainout prescription of Burrows & Sharp (1999) to account for condensation and settling in a gravitational field. Elemental solar abundances are assumed.

2.4. Reflection off an EGP Atmosphere

Since the nature of the reflection of stellar light from an EGP atmosphere determines the planetary phase function, we explore the reflection properties in some detail. Reflected light from giant planets is due to Rayleigh scattering by gases and/or scattering by the condensates in a planet’s atmosphere. We illustrate the dependence of the optical ($0.55 \mu\text{m}$) reflection coefficient on angle of incidence (which corresponds to planetary latitude and longitude according to eq. (1)) and the presence or absence of clouds in the upper atmosphere. Figures 3a through 3d show the reflection coefficient (ρ) versus the cosine of the emergent angle (μ) with respect to the normal and the azimuthal angle (ϕ) for a given incident angle (the cosine of which is represented by μ_0). Figure 3a depicts ρ for a moderate incident angle ($\mu_0=0.9$, which is $\sim 26^\circ$ from the normal to the surface) for an atmosphere with an ammonia cloud layer (modal particle size of $50 \mu\text{m}$). For such an incident angle, a backscatter peak is evident, but there is only a modest variation overall with μ and ϕ in the reflection coefficient. This result contrasts sharply with that for an oblique angle of incidence ($\mu_0 = 0.1$; Fig. 3b; note the vertical scale change), where the emergence at oblique angles is much stronger than along the normal to the surface. Also, reflection off the surface in the forward direction ($\phi = 0^\circ$) is significantly stronger than in the backward direction ($\phi = 180^\circ$). How do these scattering results compare with those for a cloud-free atmosphere? For the $\mu_0 = 0.9$ cloud-free case (Fig. 3c), the reflection coefficient again does not vary enormously with μ and ϕ , although it is clear that more radiation emerges at oblique angles than along the normal. In the $\mu_0 = 0.1$ cloud-free case, radiation scatters very obliquely, but unlike the cloudy case, scattering in the forward and backward directions off the surface is nearly equivalent.

In general, for radiation incident at angles relatively close to the normal, the scattering will not vary greatly as a function of μ or ϕ , but it varies enough that Lambert (i.e., isotropic) reflection is a poor approximation. For more oblique angles of incidence, forward and backward scattering off the surface dominates, with very little reflection into angles near the normal to the surface. For such oblique angles of incidence, the forward and backward emergence off the surface is nearly equivalent in the cloud-free case, but the forward scattering is significantly stronger in the cloudy case. Of course, this is all a function of wavelength as well, and so the problem is somewhat more complex than we can present in this subsection. Various gaseous and condensed species will affect the magnitude of the reflection coefficient, depending upon cloud scattering albedos and gaseous

absorption bands.

3. Solar System Phase Functions

The classical planetary phase function indicates the fraction of light, relative to full phase, received by a distant observer from a planet as a function of its phase angle. Measurements of phase functions for objects in our Solar System precede even the earliest space missions. However, sufficient phase data could not be obtained for the outer planets before such missions, due to the fundamental limitations of our vantage point from Earth.

Figure 4 depicts optical phase functions, $\Phi(\alpha)$, for a selection of Solar System objects along with that of a Lambert model. By definition, the classical phase function is normalized to unity at full phase. Hence, no albedo information is given in this figure, but it is useful in understanding the nature of the scattering itself. For solid bodies with thin atmospheres, such as Mars (*red curve*; Thorpe 1976), or no atmosphere (e.g. the Moon; *gray curve*; Lane & Irvine 1973), backscattering can be significant. Near full phase the backscattering contribution is greatest, and this “opposition effect” is seen in these phase functions, which peak rather strongly near full phase. In contrast, consider the Lambert scattering case (*black dashed curve*), for which radiation is scattered isotropically off a surface regardless of its angle of incidence. In that case, the phase function is more rounded near full phase. Lambert scattering appears to be a fair approximation for some objects, such as Uranus (*green curve*; Pollack *et al.* 1986), although such isotropic reflection is not manifested by any real object. Note that isotropic reflection off a surface should not be confused with an isotropic single-particle *scattering* phase function. The latter generally does not result in isotropic reflection.

Despite the number of missions to Jupiter and Saturn, full planetary phase data were never made available. However, Dyudina *et al.* (2004) recently constructed planetary phase functions for these planets by fitting a two-term Henyey-Greenstein function to original *Pioneer* red bandpass scattering data taken at several phase angles. The only ambiguities in their resulting planetary phase functions are at phase angles greater than $\sim 150^\circ$ (crescent phase) or less than $\sim 10^\circ$ (near full phase), because no *Pioneer* data were available from these regions. Their red-bandpass phase function for Jupiter is plotted in Fig. 4.

4. EGP Phase Functions

EGP phase functions are determined essentially by the constituents of a planet’s atmosphere. Rayleigh scattering dominates purely gaseous atmospheres, while grains and ices often result in strong forward and backward scattering peaks. Our theoretical EGP optical ($\lambda = 0.55 \mu\text{m}$) phase functions are shown in Fig. 5. Included are 1- M_J , 5 Gyr planets ranging in orbital distance from 0.2 AU to 15 AU about a G2V central star. Due to a low atmospheric temperature, the model planets beyond ~ 4.5 AU contain an ammonia cloud layer above a deeper water cloud deck (i.e., class

I; Sudarsky, Burrows, & Pinto 2000; Sudarsky, Burrows, & Hubeny 2003; Burrows, Sudarsky, & Hubeny 2004). Unlike Jupiter and Saturn, virtually all currently known EGPs, including the long-period Epsilon Eridani and 55 Cancri planets, likely are too warm to contain condensed ammonia (Sudarsky, Burrows, & Hubeny 2003; Burrows, Sudarsky, Hubeny 2004). However, these wide-separation EGPs will contain condensed H₂O (i.e. class II), as do our models shown at 2 AU and 4 AU. The theoretical phase functions for our baseline cloudy EGP models peak (to varying degrees) near full phase in the optical, the so-called “opposition effect.”

An EGP phase function is a wavelength-dependent quantity. Figure 6 shows this dependence between 0.45 μm and 1.25 μm for our model EGP at 8 AU. The general shape of the phase function is a function of the depth dependence of the scattering and absorption opacities, which is a complex function of wavelength. The wavelength dependence for a cloud-free model at 0.5 AU is shown in Fig. 7. Note that the 1.05 μm and 1.25 μm phase curves are outliers because they contain a mix of thermally re-emitted and reflected radiation.

5. Albedos

The albedos of EGPs vary substantially, both as a function of orbital distance and wavelength. Figure 8 depicts low resolution, wavelength-dependent spherical albedos of $1-M_J$, 5-Gyr EGPs ranging in orbital distance from 0.2 AU to 15 AU about a G2V star. The planets beyond 1 AU, with upper atmospheric water or ammonia cloud decks, exhibit the largest optical albedos. At smaller orbital radii, the optical albedos decrease, due to an absence of reflective condensates and the strengthening of atomic sodium and potassium absorption. The closest orbit in our model set is 0.2 AU. With very deep silicate and iron clouds, this object is essentially cloud-free, as are the other EGPs out to ~ 1.5 AU. The albedos for objects shown with orbital radii of 1 AU or less appear to rise into the near infrared. This effect is not due to increased reflectivity at longer wavelengths. Rather, it is a result of the object’s thermal re-emission of absorbed stellar flux. The absence of high-altitude clouds combined with strong sodium and potassium opacity keeps the optical albedo low out to a few tenths of an AU. However, with increasing orbital radius, the atmospheric temperatures drop and the alkali metals condense into chlorides (KCl) and sulfides (Na₂S), which rain out (Burrows & Sharp 1999), giving way to reflective Rayleigh scattering. Hence, the optical albedo rises significantly with increasing orbital radius between ~ 0.2 AU and 1 AU (see Fig. 8), even though there are no water clouds present. With the onset of water clouds, the optical albedo rises further still, which is seen clearly in the model at 2 AU. The onset and thickening of reflective ammonia clouds at larger orbital distances results in the highest albedos at most optical and near-infrared wavelengths.

The geometric albedo is obtained by taking the quotient of the spherical albedo and the wavelength-dependent phase integral. Figure 9 depicts cubic spline fits to the phase integral (q) for each model EGP. The phase integral varies widely as a function of wavelength and orbital distance. Cloudy atmospheres tend to have smaller phase integrals due to backscattering effects.

Our resulting geometric albedos are shown in Fig. 10. For comparison, perfect Lambert reflection (isotropic reflection with no absorption) off a sphere results in a geometric albedo of $\frac{2}{3}$, while it is $\frac{3}{4}$ for pure Rayleigh scattering.

6. Light Curves for Circular Orbits

Throughout its orbit, an EGP will exhibit different phases with respect to the observer. For simplicity, in this section we consider an idealized case of a circular, highly-inclined orbit of 80° . (An inclination of 90° is edge-on.) Section 9 investigates the effects of varying the classical orbital parameters, such as eccentricity, inclination, argument of periastron, and longitude of the ascending node.

The planet/star flux ratio (eq. 8) is an important quantity that, along with angular separation, determines the detectability of EGPs (Trauger *et al.* 2000, 2001). Due to reflective Rayleigh scattering and/or condensate clouds at altitude, the optical spectral region tends to reflect significantly more starlight than the red/infrared region. Here, we do not model non-LTE photochemical effects, which may produce species that somewhat reduce reflection in the UV/blue portion of the spectrum (e.g., Jupiter). Therefore, we shall highlight wavelengths longer than $0.5 \mu\text{m}$.

The planet/star flux ratio in the optical is determined almost entirely by reflected starlight off an EGP atmosphere. However, such is not the case in the infrared, where thermally re-emitted radiation, combined with some reflection due to clouds, will determine the ratio. Hence, although an optical EGP spectrum is expected to be fully phase-dependent, this may not be the case in the infrared, where emission may be more isotropic, depending on the efficiency of advection of heat to the night side of the planet. For the hotter EGPs ($a \lesssim 1 \text{ AU}$), the near-infrared is likely to be a combination of reflection and thermally re-emitted radiation. These components cannot easily be disentangled in a consistent manner by observations. In the near-IR, the accuracy of our theoretical light curves for hot EGPs may be diminished for phase angles that are far from full phase, because we do not account for thermal emission from planetary longitudes that are not illuminated by the central star (the “night side” of the planet).

Figure 11 shows light curves at $0.55 \mu\text{m}$, $0.75 \mu\text{m}$, and $1 \mu\text{m}$ for our model EGPs in circular orbits at 1 AU, 2 AU, and 4 AU about a G2V star (5 Gyr). The orbital inclination is set to 80° . The models at 2 AU and 4 AU contain water clouds in their upper atmospheres, while the 1 AU model does not. The planet/star flux ratios at full phase range from nearly 5×10^{-8} at $0.55 \mu\text{m}$ for the planet at 1 AU to $\sim 10^{-9}$ at $1 \mu\text{m}$ for the 4 AU planet. In addition to their magnitudes, the shapes of the light curves vary significantly. For example, the 1 AU model light curve is broader at $1 \mu\text{m}$ than at shorter wavelengths, an effect due to the mixing of some thermally re-emitted light with the reflected starlight (as discussed above). The 2 AU and 4 AU light curve shapes vary substantially as well, not due to thermal effects, but because of the strong wavelength dependence of forward scattering off water clouds. In Fig. 11, the effects of clouds can be discerned by noting

the full-phase flux levels at any wavelength for which there is no contribution from thermal re-emission. Comparing the planet/star flux ratios of the 1 AU and 2 AU models at $0.55 \mu\text{m}$ (or at $0.75 \mu\text{m}$), the brightening of the 2 AU model due to its water clouds is evident, since applying the inverse square law to the cloud-free (1 AU) model would produce a significantly lower flux ratio if it were repositioned at 2 AU.

At $0.55 \mu\text{m}$ and $0.75 \mu\text{m}$, the planet/star flux ratio near full phase is 3 to 4 times its value at greatest elongation (its maximum angular separation as seen from Earth). In the near-infrared, the variation from greatest elongation to full phase is much smaller.

The light curves for $1-M_J$, 5 Gyr ammonia class EGPs (class I) at 6 AU, 10 AU, and 15 AU about a G2V star are shown in Fig. 12. The largest planet/star flux ratios are in the optical, where an EGP at 6 AU reaches a ratio of nearly 2.5×10^{-9} and our model at 15 AU reaches a value close to 5×10^{-10} . At $1 \mu\text{m}$, the peak planet/star flux ratios are $\sim 20\text{-}40\%$ of their optical values. As with the EGPs at 1 AU, 2 AU, and 4 AU, these EGPs with larger orbital radii have planet/star flux ratios that vary by a factor of 3 to 4 in the optical from greatest elongation to near full phase.

The planet/star flux ratio as a function of orbital distance at $0.55 \mu\text{m}$, $0.75 \mu\text{m}$, $1 \mu\text{m}$, and $1.25 \mu\text{m}$ assuming a G2V central star is shown in Fig. 13. In each case, the plotted value corresponds to a planet at greatest elongation with an orbital inclination of 80° . For EGPs with relatively small orbital radii ($\lesssim 1$ AU), the near-IR flux ratios are large, due to thermal re-emission of absorbed stellar radiation at these wavelengths. With increasing orbital radius, the peak of this thermal re-emission moves to longer and longer wavelengths. This effect coupled with the condensation of reflective clouds beyond ~ 1.5 AU results in larger optical flux ratios relative to infrared flux ratios for larger orbital radii. Note that the planet/star flux ratios do not follow a simple $1/a^2$ law.

Explicitly averaging our present light curves with respect to phase, we test the validity of the previous “phase-averaged” planet/star flux ratios derived by Sudarsky, Burrows, & Hubeny (2003) and by Burrows, Sudarsky, & Hubeny (2004), for which a 1-D atmosphere code was used. Our new phase-averaged results agree quite closely with those from our previous 1-D treatment, differing by less than 3% in most cases.

7. Color Dependence with Planetary Phase

As shown in §5, EGP phase functions vary with wavelength. An interesting consequence of this fact is that an EGP is expected to show color variations throughout the different phases of its orbit. Figure 14 is a $V - R$ vs. $R - I$ color-color diagram, which details these color variations with planetary phase for a variety of orbital distances. Each of the curves in Fig. 14 covers an orbit from full phase (0°) to a thin crescent phase (170°) in increments of 10° (as indicated by the filled circles). For most cloud-free EGPs, the phase that is bluest in both $V - R$ and in $R - I$ is 80° or 90° . That is, cloud-free EGPs are bluest near greatest elongation. In comparison, EGPs with water clouds and/or ammonia clouds tend to be bluest in a gibbous phase. As full phase is approached,

the colors redden somewhat. However, the crescent phases appear to be far redder, varying by as much as a full astronomical magnitude in some cases. Bluer light scatters more efficiently via Rayleigh scattering or cloud reflection than red/infrared radiation, so an observer viewing an EGP at an intermediate phase will catch more blue photons than an observer of a crescent phase, for which the bluer photons have been scattered away from the line of sight.

The cloud-free 1 AU model shown in Fig. 14 deviates significantly in color space from the 2 AU (water cloud), 6 AU, 10 AU, and 15 AU models (with ammonia and water clouds). The cloudy models are substantially redder in both $V - R$ and $R - I$. Additionally, the excursion in $R - I$ is much smaller for the cloud-free model. This is not surprising, given that Rayleigh scattering ($\propto \lambda^{-4}$) is far less effective than condensate scattering in this region of the spectrum. Still, in $V - R$, the cloud-free 1 AU model is expected to vary with phase by as much as 0.5 magnitude.

Due to our use of a 2-D planar code, we cannot model limb effects, such as transmission of stellar radiation through a chord of the atmosphere. Although we are confident in the color trends of Fig. 14, the values at very large phase angles may not be as robustly calculated as the rest. We have denoted uncertain areas of this diagram with dotted lines. Note that EGP direct imaging at such large phase angles would be very difficult in these wavelength bands, due to the lower planet/star flux ratios at crescent phases and the associated small angular separation from the star.

8. Condensate Particle Size Dependence

Modeling cloud particle sizes in EGP atmospheres remains a difficult endeavor. The phase functions and light curves presented thus far have been produced using the prescription of Cooper *et al.* (2003). While their resulting particle sizes are in broad agreement with those of others (Ackerman & Marley 2001; Lunine *et al.* 1989), we recognize that cloud formation in EGPs is a complex process, which may not be reproduced correctly by current modeling algorithms. Furthermore, for simplicity, in this paper we hold the modal particle size constant throughout the cloud layer, using the particle size at the cloud base. In reality, particle sizes may tend to decrease somewhat toward the cloud tops, an effect that we have not incorporated. Hence, we explore the effects of significant cloud particle size variation on our EGP phase functions.

Figure 15 depicts the Mie theory optical angular scattering dependence of H₂O ice, NH₃ ice, and forsterite grains at modal particle sizes of 1 μm , 10 μm , and 100 μm . Our derived particle sizes are generally encompassed by this broad range. Most of our ammonia and (especially) water cloud modal particle sizes fall near the upper end of the range. In Fig. 15, the usual Deirmendjian (1964) size distribution function is used. The data are fit with cubic splines and offset for clarity. For all species, the angular distribution exhibits a strong forward peak at small scattering angles. This peak strengthens with increasing particle size and is quite extreme at 100 μm . Additionally, a significant backscatter peak is common, an effect that cannot be represented by the commonly

used Henyey-Greenstein scattering phase function.

We explore the dependence of EGP light curves on condensate particle sizes in Fig. 16 for the optical wavelength of $0.55 \mu\text{m}$, and in Fig. 17 at $0.75 \mu\text{m}$. In each figure, model light curves for EGPs at 2 AU with modal H_2O ice particle sizes of 1, 3, 10, 30, and $100 \mu\text{m}$ are depicted. Shown for comparison is a cloud-free model (*black dashed curve*). In order to show the full variation with particle size in the shapes and magnitudes of the light curves, we have set the orbital inclination to $\sim 90^\circ$ so that the opposition effect, present for many of the models, can be seen in full (transit effects are ignored). Use of Mie scattering theory is necessary in order to derive the wavelength-dependent scattering properties for various cloud particle sizes, but smaller particle sizes generally result in higher planet/star flux ratios at most wavelengths. Scattering cross sections are roughly proportional to the square of the particle size, but the number density of particles for a given condensate mass scales as the inverse cube of the size. Hence, the total cloud scattering opacity tends to be greater for smaller particles at most wavelengths.

At both $0.55 \mu\text{m}$ and $0.75 \mu\text{m}$, the $1 \mu\text{m}$ particle size models exhibit higher planet/star flux ratios and smoother light curves than for those models with larger particles. At $0.55 \mu\text{m}$, the planet/star flux ratios do not vary substantially over a range of modal particle sizes from 3 to $100 \mu\text{m}$ (although the shapes of the light curves differ somewhat). This result contrasts with those of the same EGPs at $0.75 \mu\text{m}$, where the planet/star flux ratio becomes progressively lower with increasing particle size. Such results indicate the importance not only of condensate particle size, but of wavelength-dependent light curves as well.

9. Elliptical Orbits and Dependence on Orientation

Until now, we have chosen to limit our discussion of EGP phase functions to nearly edge-on circular orbits. In reality, EGP orbital inclinations are randomly distributed, and elliptical orbits are prevalent for all but the close-in EGPs. An observer’s viewing angle affects the range of phases visible, and the eccentricity and semi-major axis determine the duration of each phase throughout the orbital period. Strikingly, a significant eccentricity can lead to a compositional difference in a planet’s atmosphere, because the level of heating from its central star varies greatly. We investigate the effects of such changes on the phase functions and light curves of EGPs.

9.1. Cloud-Free Elliptical Orbits

The light curve of a planet in an eccentric orbit will be very different from that of the same planet in a circular orbit. In the cloud-free case, this difference is due largely to the amount of time the planet spends at a given phase in its orbit and the varying distance of the planet to its central star at a given phase.

Dyudina et al. (2004) pointed out that the peak of the light curve for an eccentric orbit does not occur at full phase. This actually is an effect of the observer viewing angle and is a function of the argument of periastron, the longitude of the ascending node, and the orbital eccentricity. Assuming a default Ω of 90° , the peak does occur at full phase for $\omega = 90^\circ$ or 270° , but otherwise does not.

Figure 18 depicts the optical light curves of orbits with various eccentricities for a cloud-free EGP orbiting a G2V star. The semi-major axis is set to 1 AU, leading to an orbital period of 1 year. We use the default values of $\Omega = 90^\circ$, $\omega = 0^\circ$ (and $i = 90^\circ$ so that full phase can be represented), resulting in a light curve whose peak value leads the full phase of the planet. This is because the orbital distance increases before full phase is reached. In this figure, the time of full phase is indicated for each orbit by a filled circle. Only for a circular orbit does the peak of the light curve match up with the time that the planet reaches full phase. For $e=0.2$, full phase lags the light curve peak by 13.7 days. For $e=0.4$, the lag is 18.2 days, while for $e=0.6$ it is 13.5 days, given our orbital parameter assumptions. The value of the light curve maximum varies greatly with orbital eccentricity because the incident stellar flux on the planet increases by a factor of $(1+e)^2(1-e)^{-2}$ between apastron and periastron.

9.2. Condensation and Sublimation Transitions in Elliptical Orbits

The presence or absence of condensate clouds in the outer atmosphere of an EGP depends largely on the level of stellar radiation incident on the planet. A cloud base resides approximately where the condensation curve of a given species intersects the atmospheric T-P profile, but the T-P profile itself is coupled strongly to the intensity of the incident radiation. Even for eccentricities of 0.2 or 0.3, the incident fluxes differ enough that an EGP may be virtually cloud-free at periastron, but have substantial water condensation at apastron. This “switching” of EGP composition classes will have visible effects in the light curves of such planets. We model these eccentric orbits by interpolating the albedo and phase spectra within our grid of circular EGP orbit results between 0.2 and 15 AU. Hence, we assume that the timescale of the chemistry associated with cloud formation and sublimation is much shorter than a planetary orbital period.

Figure 19 depicts optical light curves for an EGP with $a=1.5$ AU and $e=0.3$, assuming a G2V central star (a system similar to HD 160691; Jones *et al.* 2002). Three different possible viewing angles are shown (*solid curves*). For the sake of comparison, also shown are the light curves that would result if the object were to remain cloud-free throughout its entire orbit (*dashed curves*), which is not expected to be the case in reality. To keep things simple, we have fixed i at 80° and Ω at 90° . For the three values of ω shown, both the 0° and 270° viewing angles exhibit pronounced effects due to the condensation of water. At $\omega = 270^\circ$, the full phase difference between our actual model with water condensation and one that artificially remains cloud-free is nearly a factor of 2 in the planet/star flux ratio. In general, the peak level of this ratio also depends on the orbital distance of the planet near full phase. In fact, its value is actually greatest for $\omega = 90^\circ$ because full

phase is reached at periastron. Due to the increased stellar heating at this phase and viewing angle, water does not condense, but such condensation does have a small effect as the orbit progresses toward greatest elongation. Clearly, the functional dependence of an EGP light curve on observer viewing angle and cloud condensation can be quite complex.

An EGP in a near-circular 4-AU orbit about a G2V star contains a tropospheric water cloud deck. With increasing eccentricity, ammonia condenses above the water cloud deck when the planet is near apastron, resulting in a two-cloud atmosphere. As the planet orbits back toward periastron, the ammonia cloud sublimates, leaving only the water cloud layer. Figure 20 depicts planet/star flux ratios (note log scale) as a function of eccentricity for $a = 4$ AU, including the effects of cloud condensation and fixing i at 80° , Ω at 90° , and ω at 0° . We plot these flux ratios in the optical ($0.55 \mu\text{m}$) and at $0.75 \mu\text{m}$. Although the $0.75 \mu\text{m}$ region has the highest-albedo beyond $0.7 \mu\text{m}$ for most EGPs, the planet/star flux ratio is still a factor of 2 to 3 below that in the optical region at most planetary phases, which indicates that the near-IR may be a more difficult spectral region in which to detect reflected-light EGPs. The periodic variation in atmospheric composition (i.e. the appearance and disappearance of the ammonia cloud layer above the water cloud layer) has a less extreme effect on the light curve than does the variation between cloudy and cloud-free for the $a=1.5$ AU EGP discussed above.

9.3. Effects of Inclination and Longitude of Ascending Node

By fixing the inclination of each orbit at 80° or 90° , we have been showing upper limits to the variation in planet/star flux ratios. In Fig. 21, we illustrate how the light curve of an elliptical orbit varies with inclination, given $\Omega = 90^\circ$. The optical peak planet/star flux ratio of an EGP with $a = 1.5$ AU and $e = 0.3$ orbiting a G2V star differs by as much as a factor of 3 over the full range of $i = 0^\circ$ to $i = 90^\circ$. There is variation in the light curve even for the face-on $i = 0^\circ$ case, an effect that is due entirely to the change in the planet-star distance for this eccentric orbit.

We explore the effect on the light curve of varying the value of the longitude of the ascending node from its default value of 90° . Recall that this parameter is the angle between the observer’s line of sight and the line formed by the intersection of the observer’s plane and the orbital plane (the line of nodes). As this angle decreases from 90° to 0° (or increases from 90° to 180°), the EGP orbit becomes edge-on, irrespective of the orbital inclination, because the line of nodes becomes parallel to the observer’s line of sight. Figure 22 shows the optical light curve for several different values of Ω for our $a = 1.5$ AU, $e = 0.3$, $i = 60^\circ$ EGP. The maximum of the light curve shifts from ~ 0.25 years for $\Omega = 90^\circ$ to ~ 0.9 years (half the orbital period) for $\Omega = 0^\circ$. For this particular set of parameters, the maximum planet/star flux ratio also decreases with Ω , until $\Omega = 0^\circ$ is approached, where the opposition effect produces a distinct peak at full phase.

10. Summary and Prospects for Detection

Our suite of model EGP phase functions and light curves from 0.2 AU to 15 AU covers a large variation in atmospheric composition, from deep silicate cloud and cloud-free EGPs with alkali metals, to giant planets with clouds of frozen ammonia particles. Self-consistent, wavelength-dependent modeling of EGP phase functions, albedos and light curves reveals that:

- Albedos and phase integrals of EGPs are strongly wavelength-dependent. Most EGPs reflect incident light to a larger degree in the optical than in the red or near-IR.
- Planetary phase functions are wavelength-dependent. Such differences with wavelength result in color differences for a given EGP throughout the various phases of its orbit. In $V - R$ and $R - I$, cloud-free EGPs are bluest near greatest elongation, while cloudy (water and/or ammonia) EGPs tend to be bluest in a gibbous phase.
- Cloud-free EGPs exhibit smooth phase functions and light curves with no significant “opposition effect.” Cloudy EGPs may or may not exhibit an opposition effect, depending on cloud particle sizes. Only for nearly edge-on orbits would such an effect be seen.
- Small cloud particle sizes ($\sim 1 \mu\text{m}$) produce higher planet/star flux ratios than large particle sizes ($\sim 100 \mu\text{m}$) at most optical and near-IR wavelengths. Furthermore, the shapes of cloudy EGP light curves depend on both particle size and wavelength.
- Assuming highly-inclined circular orbits, at optical wavelengths EGPs are 3 to 4 times brighter near full phase than near greatest elongation.
- EGPs in elliptical orbits can undergo major atmospheric compositional changes, which may have significant effects on their light curves. Additionally, elliptical orbits generally introduce an offset between the time of the light curve peak and the time of full planetary phase.
- Because most wide-separation EGPs are in elliptical orbits, the Keplerian elements, such as inclination, argument of periastron, and longitude of the ascending node, play important roles in the shapes of their light curves.
- The previous “phase averaged” planet/star flux ratios of Sudarsky, Burrows, & Hubeny (2003) and Burrows, Sudarsky, & Hubeny (2004), derived with a 1-D atmosphere code, are accurate to within 3% in most cases.

The direct imaging of wide-separation EGPs at optical wavelengths, a lofty goal by any measure, may become possible within the next several years by high contrast, space-based imaging instruments such as *Eclipse* (Trauger *et al.* 2000, 2001) or *EPIC* (Clampin *et al.* 2002; Lyon *et al.* 2003). *Eclipse* is a 1.8-meter optical and near-infrared telescope with an adaptive optics system. High contrast imaging of $\sim 10^9$ in the optical, given an angular separation of $0.3''$ - $2''$, may be possible. If such sensitivity materializes, then a number of EGPs may be detectable. For example, an EGP in

a 4-AU orbit about a G2V star at 10 parsecs has an angular separation as large as $0.4''$, and just beyond greatest elongation (in a gibbous phase) it is expected to exhibit an optical planet/star contrast above $\sim 2 \times 10^{-9}$ (see Fig. 11). Even at 6 AU, and in this same phase, the planet-star contrast in the optical is expected to be roughly 10^{-9} . Detailed models of specific EGP systems in combination with reliable ephemerides are necessary both in the selection of good targets and for the physical interpretation of positive observational results.

The authors are happy to thank Bill Hubbard, Jonathan Lunine, Christopher Sharp, and Drew Milsom for insightful conversations and help during the course of this work, as well as NASA for its financial support via grants NAG5-10760 and NNG04GL22G. Furthermore, we acknowledge support through the Cooperative Agreement NNA04CC07A between the University of Arizona/NOAO LAPLACE node and NASA’s Astrobiology Institute.

A. Appendix

We solve the radiative transfer equation,

$$\mu \frac{dI(\nu, \mu, \phi)}{dz} = -\chi(\nu)[I(\nu, \mu, \phi) - S(\nu, \mu, \phi)], \quad (\text{A1})$$

where I is the specific intensity of radiation at frequency ν , and the direction is specified by θ and ϕ , where θ is the angle with respect to the normal to the surface ($\mu = \cos \theta$), and ϕ is the azimuthal angle. Furthermore, z is the geometrical coordinate, χ is the total extinction coefficient, and S the source function, which in the present case is given by

$$S(\nu, \mu, \phi) = \frac{1 - \epsilon_\nu}{4\pi} \int_{-1}^1 d\mu' \int_0^{2\pi} d\phi' I(\nu, \mu', \phi') g(\nu, \mu', \phi', \mu, \phi) + \epsilon_\nu B_\nu, \quad (\text{A2})$$

where $1 - \epsilon_\nu$ is the single-scattering albedo and ϵ_ν is the photon destruction coefficient, given by

$$\epsilon_\nu = \frac{\kappa_\nu}{\chi_\nu} \equiv \frac{\kappa_\nu}{\sigma_\nu + \kappa_\nu}, \quad (\text{A3})$$

where κ_ν is the coefficient of true absorption, and σ_ν the scattering coefficient. Function $g(\nu, \mu', \phi', \mu, \phi)$ describes a change of direction of a scattered photon, and is called the phase function, or the single-scattering phase function.

The transfer equation (A1) does not involve a coupling of the individual frequencies; a solution may then be done frequency by frequency. In the following text, we omit an explicit indication of the frequency dependence. Introducing the optical depth,

$$d\tau = -\chi dz, \quad (\text{A4})$$

we rewrite the transfer equation (A1) in the usual form,

$$\mu \frac{dI(\mu, \phi)}{d\tau} = I(\mu, \phi) - S(\mu, \phi). \quad (\text{A5})$$

For a numerical solution of eq. (A1) with the angle-dependent source function eq. (A2), we discretize the optical depth and both angles, $\{\tau_d, d = 1, \dots, ND\}$, $\{\mu_i, i = 1, \dots, NMU\}$, and $\{\phi_j, j = 1, \dots, NPHI\}$, and replace the integral in the source function eq. (A2) by a quadrature sum,

$$S_{i,j} = (1 - \epsilon) \sum_{k=1}^{NMU} \sum_{l=1}^{NPHI} I_{k,l} g_{k,l,i,j} w_k^\mu w_l^\phi, \quad (\text{A6})$$

where $I_{k,l} \equiv I(\mu_k, \phi_l)$, and w^μ and w^ϕ are the quadrature weights for the integrals over μ and ϕ , respectively.

The transfer equation (A5) is supplemented by the boundary conditions. At the lower boundary, we assume the diffusion approximation,

$$I(\mu, \phi) = B + \mu \frac{dB}{d\tau}, \quad \text{for } \mu > 0, \quad (\text{A7})$$

where B is the Planck specific intensity. At the surface we have

$$I(\mu, \phi) = I^{\text{ext}}(\mu, \phi), \quad \text{for } \mu < 0, \quad (\text{A8})$$

where I^{ext} is the specific intensity of the external radiation. In the case of a point source, the external intensity is given by

$$I^{\text{ext}}(\mu, \phi) = I^0 \delta(\mu - \mu^0) \delta(\phi), \quad (\text{A9})$$

where δ is the Dirac δ -function. Thus, we consider the external source at $\mu = \mu^0$ and $\phi = 0$.

There are two different approaches to solve equation (A5) with the source function eq. (A6): a direct one, and an iterative one. Sudarsky, Burrows, & Pinto (2000) considered an azimuthally-averaged specific intensity and redistribution function so that their specific intensity depended on only one angle, $I = I(\mu)$ and $g = g(\mu', \mu)$. They solved eq. (A1) with an appropriately modified eq. (A2) using the Feautrier method (e.g., Mihalas 1978). This direct method solves for the angular coupling directly, but at the expense of inverting an $NMU \times NMU$ matrix at each discretized depth point.

Generalizing a direct scheme to handle a dependence on two angles would be very cumbersome and computationally costly, so we have developed another, much faster, scheme based on the Accelerated Lambda Iteration method (ALI). Let us first take the simpler case of isotropic scattering. In this case, the source function is given by

$$S = (1 - \epsilon)J + \epsilon B, \quad (\text{A10})$$

where

$$J \equiv \frac{1}{4\pi} \int_{-1}^1 \int_0^{2\pi} I(\mu, \phi) d\mu d\phi \quad (\text{A11})$$

is the mean intensity of radiation. The solution of the transfer equation may be written as

$$J = \Lambda[S], \quad (\text{A12})$$

where Λ is an operator acting on the source function. Using this relation, we obtain a single operator (integral) equation for the source function,

$$S = (1 - \epsilon) \Lambda[S] + \epsilon B. \quad (\text{A13})$$

The idea of accelerating the Lambda iteration consists of writing

$$\Lambda = \Lambda^* + (\Lambda - \Lambda^*), \quad (\text{A14})$$

where Λ^* is an appropriately chosen *approximate lambda operator*. The iteration scheme for solving Eq. (A13) may then be written as

$$S^{(n+1)} = (1 - \epsilon) \Lambda^*[S^{(n+1)}] + (1 - \epsilon)(\Lambda - \Lambda^*)[S^{(n)}] + \epsilon B. \quad (\text{A15})$$

The action of the exact Λ operator is thus split into two components: an approximate Λ^* operator acting on the *new* iterate of the source function, and the difference between the exact and approximate operator, $\Lambda - \Lambda^*$, acting on the previous, *old*, and, thus, known source function. The latter contribution may be easily evaluated by the formal solution. By the term “formal solution” we mean a numerical solution of the transfer equation where the source function is fully specified.

Olson, Auer, & Buchler (1986) showed that a nearly optimum Λ^* operator is the diagonal (local) part of the exact Λ operator, which can be easily evaluated. Inversion of Λ^* is thus a simple algebraic division.

Applying the ALI idea to anisotropic scattering is not so straightforward because the source function now depends on two angles, θ and ϕ . Thus, we introduce a ratio, $a_{\mu\phi}$, of the true scattering term of the source function to the angle-averaged one,

$$a_{\mu\phi} = \frac{\int_{-1}^1 d\mu' \int_0^{2\pi} d\phi' I(\mu', \phi') g(\mu', \phi', \mu, \phi)}{4\pi J}, \quad (\text{A16})$$

and use a scheme that proceeds as two nested iteration loops:

- 1) estimate $a_{\mu\phi}$ (typically, initialize $a_{\mu\phi} = 1$);
- 2) while holding $a_{\mu\phi}$ fixed, iterate for S exactly as in the usual ALI treatment of the case of isotropic scattering;
- 3) after the inner loop is finished, update $a_{\mu\phi}$, and repeat.

The problem is thus essentially reduced to a set of formal solutions of the transfer equation along individual rays defined by angles, θ and ϕ . For the formal solution, we may use either the short characteristics method (Olson & Kunasz 1987; Hubeny 2003), or a Discontinuous Finite-Element (DFE) method (Castor, Dykema, & Klein 1992)

The single-scattering phase function, $g(\Theta)$, Θ being the scattering angle, is computed in discrete values of $\Theta = \Theta_1, \dots, \Theta_{NT}$, with $\Theta_1 = 0$ and $\Theta_{NT} = \pi$. However, in many cases the phase function

is a very strongly peaked function of Θ , with a peak at $\Theta = 0$ (forward scattering). Any simple angular quadrature thus yields inaccurate results, essentially because $g(\Theta_1 = 0)$ may be several orders of magnitude larger than $g(\Theta_2)$, even for small values of Θ_2 (in our calculations, we used $\Theta_2 = 1^\circ$). Because it is impractical to set up too many points very close to $\Theta = 0$, we devised the following procedure. We split the phase function into two components: one (g') that has the same value at $\Theta_1 = 0$ as at Θ_2 (or given by some suitable extrapolation from the values at Θ_3, Θ_4 , etc.), and the second being the Dirac delta-function $\delta(\Theta)$, viz.

$$g(\Theta) = g'(\Theta) + \alpha\delta(\Theta). \quad (\text{A17})$$

This function is properly normalized to unity,

$$\int g(\Theta)d\Theta = \int g'(\Theta)d\Theta + \alpha = 1. \quad (\text{A18})$$

Now, with this form of the phase function, one can analytically handle the source function. The scattering contribution to the source function becomes (schematically):

$$S^{\text{sct}}(\mu, \phi) = \frac{1}{4\pi} \int_{-1}^1 d\mu' \int_0^{2\pi} d\phi' I(\mu', \phi') g(\mu', \phi', \mu, \phi) \quad (\text{A19})$$

$$= \int_{-1}^1 d\mu' \int_0^{2\pi} d\phi' I(\mu', \phi') g'(\mu', \phi', \mu, \phi) + \alpha I(\mu, \phi) \quad (\text{A20})$$

and, thus, the term $\alpha I(\mu, \phi)$ can be understood as a negative contribution to the absorption coefficient. Therefore, one can use, in the angle-dependent transfer calculations, the modified phase function g' , which is smooth and well-behaved, and the scattering contribution to the absorption coefficient χ will be modified to $(1 - \alpha)\chi$. In other words, very strong forward-scattering effectively reduces the optical thickness of the cloud.

REFERENCES

- Antonello, E. & Ruiz, S. M. 2002, *The Corot Mission*, <http://www.astrsp-mrs.fr/projects/corot/corotmission.ps>
- Arnold, L. & Schneider, J. 2004, *Astron. Astrophys.*, *in press*
- Beichman, C.A., Coulter, D.R., Lindensmith, C., & Lawson, P.R. 2002, Selected Mission Architectures For The Terrestrial Planet Finder (TPF): Large, Medium, and Small. in *Future Research Direction and Visions for Astronomy*. (ed. Dressler, Alan M.), Proceedings of the SPIE, Vol. 4835, pp. 115-121
- Butler, R. P., Marcy, G. W., Williams, E., Hauser, H. & Shirts, P. 1997, *Astrophys. J. Letters*, 474, L115
- Butler, R. P., Marcy, G. W., Fischer, D. A., *et al.* 1999, *ApJ*, 526, 916

- Butler, R. P., Marcy, G. W., Vogt, S. S., Tinney, C., Jones, H., McCarthy, C., Penny, A., Apps, K., & Carter, B. 2002, *ApJ*, 578, 565
- Burrows, A., Marley, M., Hubbard, W. B., Lunine, J. I., Guillot, T., Saumon, D., Freedman, R., Sudarsky, D., & Sharp, C. 1997, *ApJ*, 491, 856
- Burrows, A. & Sharp, C. M. 1999, *ApJ*, 512, 843
- Burrows, A., Hubbard, W. B., Lunine, J. I., & Liebert, J. 2001, *Rev. Mod. Phys.*, 73, 719
- Burrows, A., Sudarsky, D., & Hubeny, I. 2004, *ApJ*, 609, 407
- Christensen-Dalsgaard, J. 2000, <http://bigcat.obs.aau.dk/hans/mons/>
- Clampin, M., Sirianni, M., Blakeslee, J. P., & Gilliland, R. L. 2002, in *Proceedings of the 2002 HST Calibration Workshop*, ed. S. Arribas, A. Koekemoer, & B. Whitmore, p. 3
- Cooper, C. S., Sudarsky, D., Milsom, J. A., Lunine, J. I., & Burrows, A. 2003, *ApJ*, 586, 1320
- Deirmendjian, D. 1964, *Applied Optics*, 3, 187
- Dyudina, U. A., Sackett, P. D., Bayliss, D. D., Seager, S., Porco, C. C., Throop, H. B., & Dones, L. 2004, [astro-ph/0406390](http://arxiv.org/abs/astro-ph/0406390)
- Green, D., Matthews, J., Seager, S., & Kuschnig, R. 2003, *ApJ*, 597, 590
- Horak, H. G. 1950, *ApJ*, 112, 445
- Hubeny, I. 2005, *in preparation*
- Hubeny, I. & Lanz, T. 1995, *ApJ*, 439, 875
- Jones, H. R. A., Butler, P. R., Marcy, G. W., Tinney, C. G., Penny, A. J., McCarthy, C., & Carter, B. D. 2002, *MNRAS*, 337, 1170
- Koch, D., Borucki, W., Webster, L., Dunham, E., Jenkins, J., Marrion, J., & Reitsema, H. 1998, *SPIE Conference 3356: Space Telescopes and Instruments V*, 599
- Lane, A. P. & Irvine, W. M. 1973, *AJ*, 78, 267
- Li, A. & Greenberg, J. M. 1997, *Astron. Astrophys.*, 323, 566
- Li, A. 2003, *ApJ*, 584, 593
- Lunine, J. I., Hubbard, W. B., Burrows, A., Wang, Y.-P., & Garlow, K. 1989, *ApJ*, 338, 314
- Lyon, R. G., Gezari, D. Y., Melnick, G. J., Nisenson, P., Papaliolios, C. D., Ridgway, S. T., Friedman, E. J., Harwit, M., & Graf, P. 2003, *SPIE Conference 4860: High-Contrast Imaging for Exo-Planet Detection*, p. 45

- Marcy, G. W. & Butler, R. P. 1996, *ApJ*, 464, L147
- Marcy, G. W., Butler, R. P., Vogt, S. S., Fischer, D., & Lissauer J. J. 1998, *Astrophys. J. Letters* , 505, L147
- Marcy, G. W., Butler, R. P., Fischer, D. A., Laughlin, G., Vogt, S. S., Henry, G. W., & Pourbaix, D. 2002, *ApJ*, 581, 1375
- Martonchik, J. V., Orton, G. S., & Appleby, J. F. 1984, *Applied Optics*, 23, 541
- Matthews, J. M., Kuschnig, R., Walker, G. A. H. *et al.* 2001, in *The Impact of Large-Scale Surveys on Pulsating Star Research*, ed. L. Szabados & D. Kurtz, p. 74
- Mayor, M. & Queloz, D. 1995, *Nature*, 378, 355
- Pollack, J. B., Rages, K., Baines, K. H., Bergstralh, J. T., Wenkert, D., & Danielson, G. E. 1986, *Icarus*, 65, 442
- Queloz, D. M., Mayor, M., Weber, L., Blecha, A., Burnet, M., Confino, B., Naef, D., Pepe, F., Santos, N., Udry, S. 2000, *Astron. Astrophys.* , 354, 99
- Scott, A. & Duley, W. W. 1996, *ApJS*, 105, 401
- Seager, S. & Sasselov, D. D. 1998, *ApJ*, 502, 157
- Seager, S., Whitney, B. A., & Sasselov, D. D. 2000, *ApJ*, 540, 504
- Sobolev, V. V. 1975, *Light Scattering in Planetary Atmospheres*, (Oxford: Pergamon Press Ltd.)
- Sudarsky, D., Burrows, A., & Pinto, P. 2000, *ApJ*, 538, 885
- Sudarsky, D., Burrows, A., & Hubeny, I. 2003, *ApJ*, 588, 1121
- Thorpe, T. E. 1976, *JGR*, 82, 4161
- Trauger, J., Backman, D., Brown, R. A. *et al.* 2000, AAS Meeting 197, 49.07
- Trauger, J., Hull, A. B., & Redding, D. A. 2001, AAS Meeting 199, 86.04
- van de Hulst, H. C. 1980, *Multiple Light Scattering Tables Formulas, and Applications*, (New York: Academic Press)
- Warren, S. G. 1984, *Applied Optics*, 23, 8
- Warren, S. G. 1991, in *Handbook of Optical Constants of Solids II*, ed. E. Palik (San Diego: Academic Press, Inc.), 236

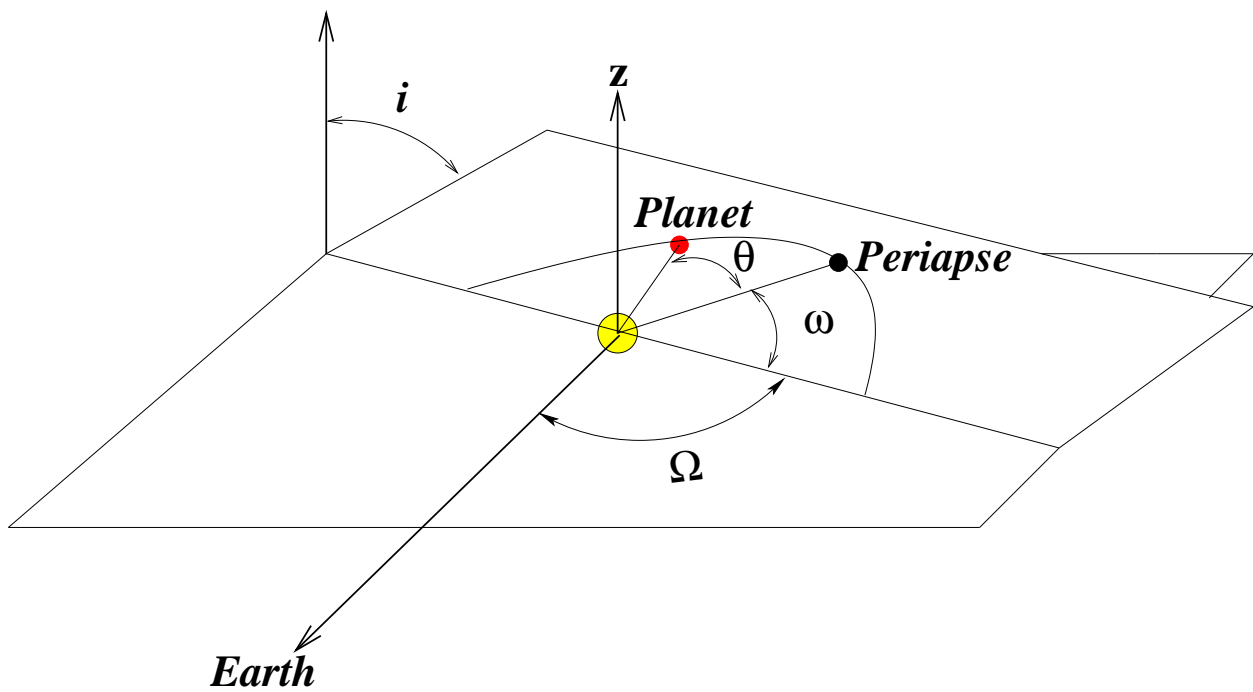


Fig. 1.— Geometry of a planet in orbit about its central star. The Keplerian elements include the inclination (i), argument of periastron or periastron (ω), longitude of the ascending node (Ω), and orbital angle or “true anomaly” (θ). See text for details.

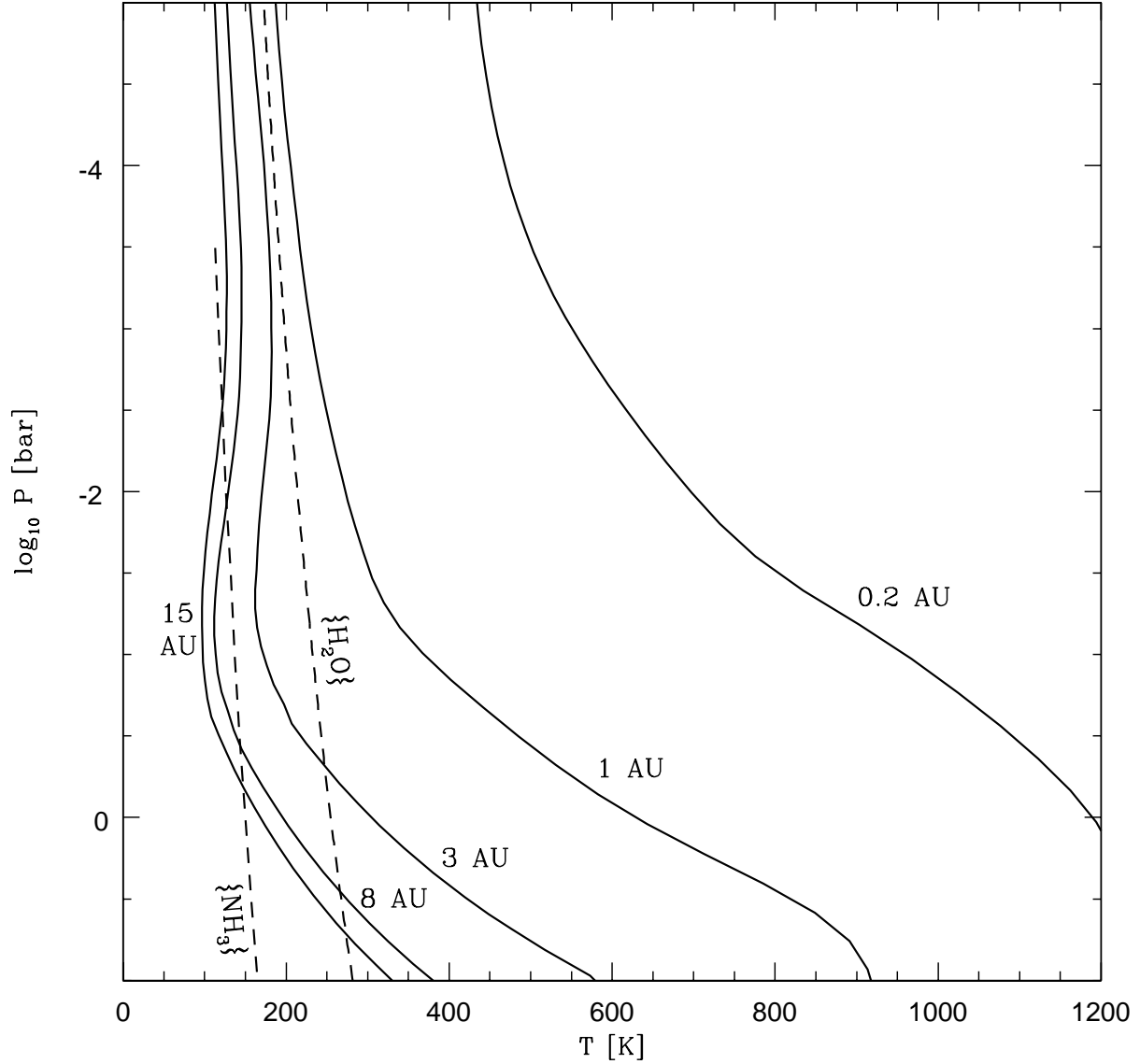


Fig. 2.— The temperature-pressure (T-P) profiles for a selection of our model EGPs. Condensation curves for water and ammonia are shown, while those for forsterite and iron are off the scale, at higher temperatures. The deeper intersections of these condensation curves with the T-P profiles indicate the positions of the cloud bases.

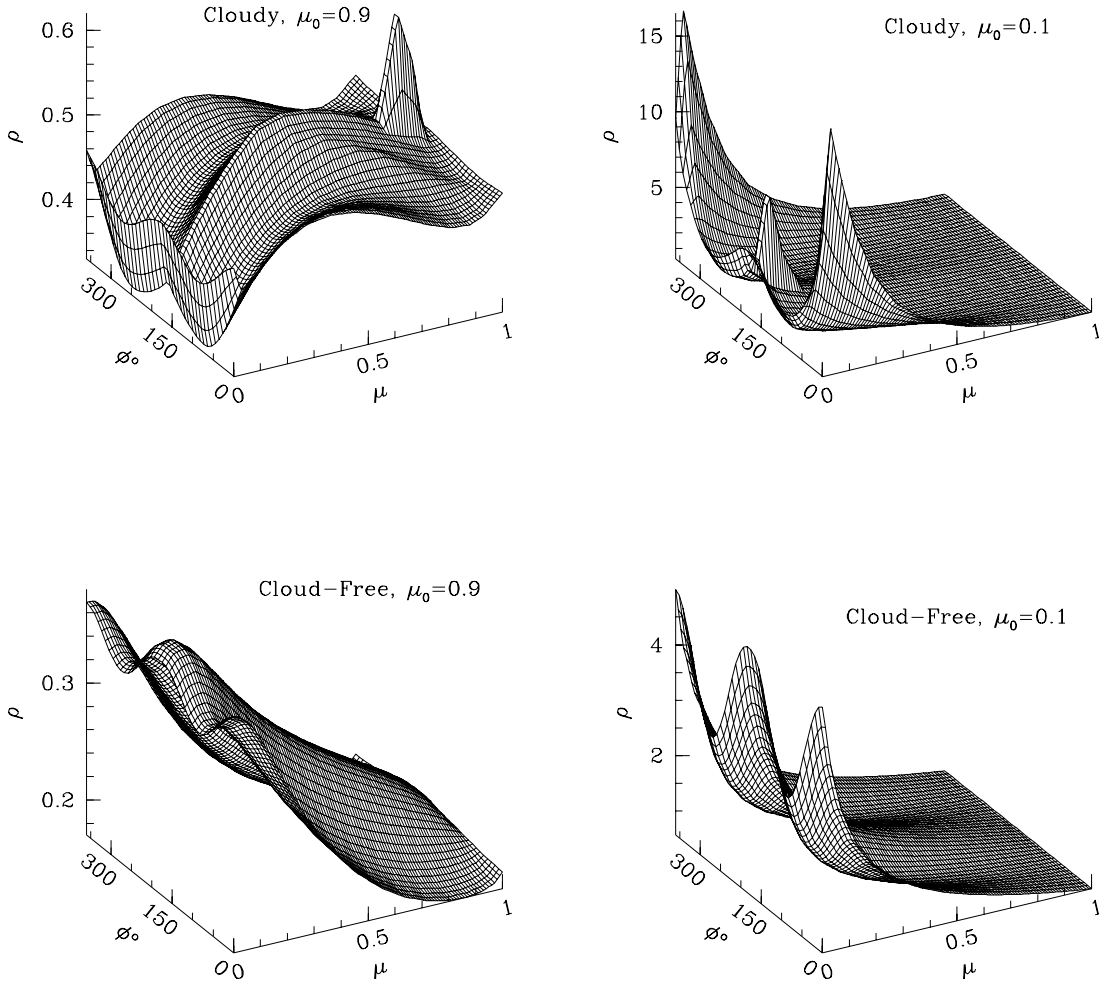


Fig. 3.— The scattering of incident $0.55 \mu\text{m}$ radiation off cloudy (condensed ammonia) and cloud-free atmospheres. For a given angle of incidence (the cosine of which is represented by μ_0) the reflection coefficient (ρ) is plotted versus the cosine of the emergent angle (μ) and the azimuthal angle (ϕ). **a: (upper left panel)** For a moderate incident angle ($\mu_0=0.9$, which is $\sim 26^\circ$ from the normal to the surface) onto a cloudy atmosphere, a backscatter peak is evident, but there is only a modest variation overall in the reflection coefficient with μ and ϕ . **b: (upper right panel)** For oblique angles of incidence, radiation emerges in a strong oblique manner at all azimuth values, but particularly in the forward direction. **c: (lower left panel)** For the $\mu_0 = 0.9$ cloud-free case, the reflection coefficient again does not vary enormously with μ and ϕ , although it is clear that more radiation emerges at oblique angles than along the normal. **d: (lower right panel)** In the $\mu_0 = 0.1$ cloud-free case, radiation scatters very obliquely, but unlike the cloudy case, the strength of the scattering in the forward and backward directions is nearly equivalent.

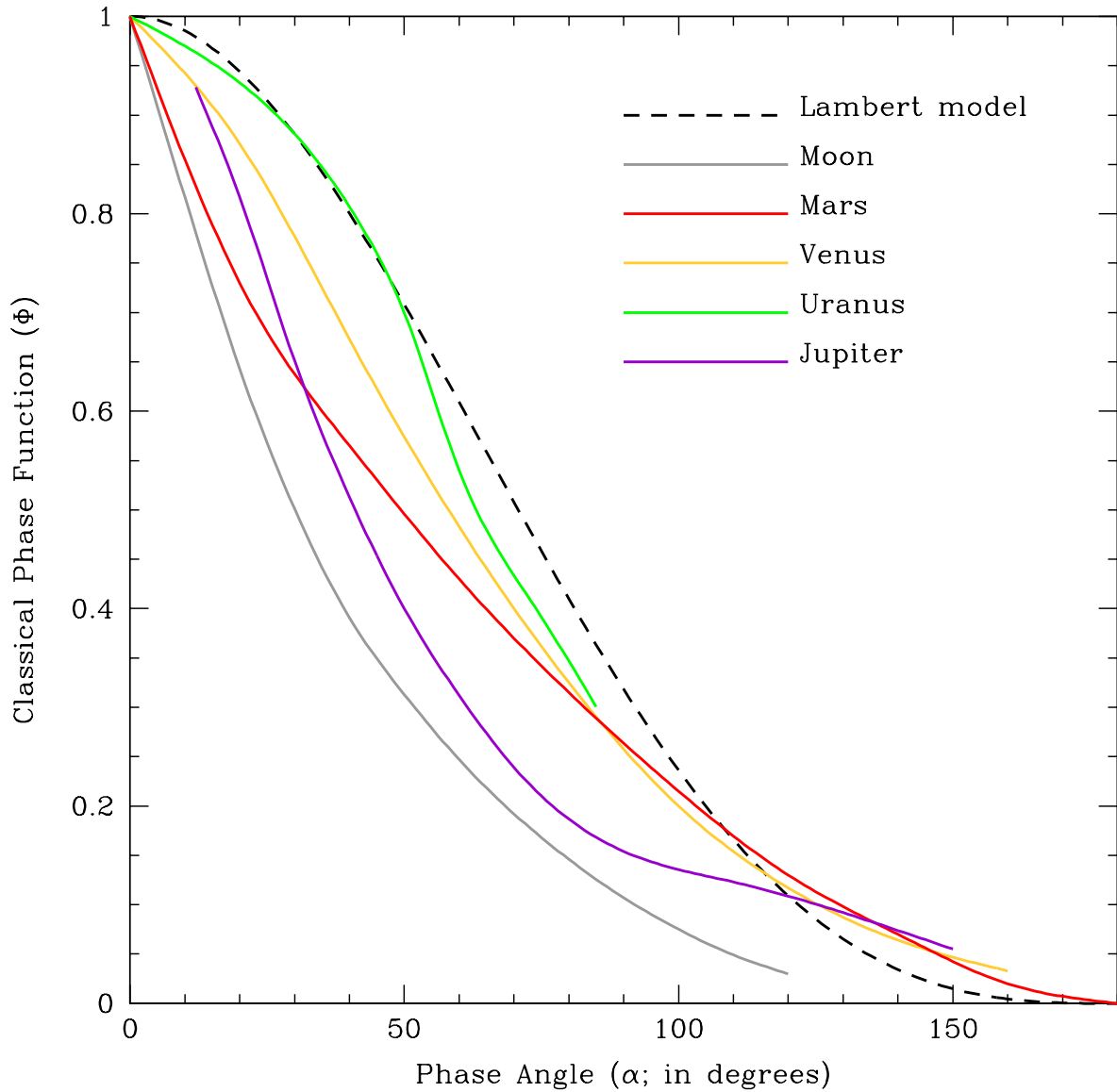


Fig. 4.— The measured visual phase functions for a selection of Solar System objects. A Lambert scattering phase curve, for which radiation is scattered isotropically off the surface regardless of its angle of incidence, is shown for comparison. The phase functions of the Moon and Mars peak near full phase (the so-called “opposition effect”). A red bandpass Jupiter phase function, taken from Dyudina *et al.* (2004), is also plotted.

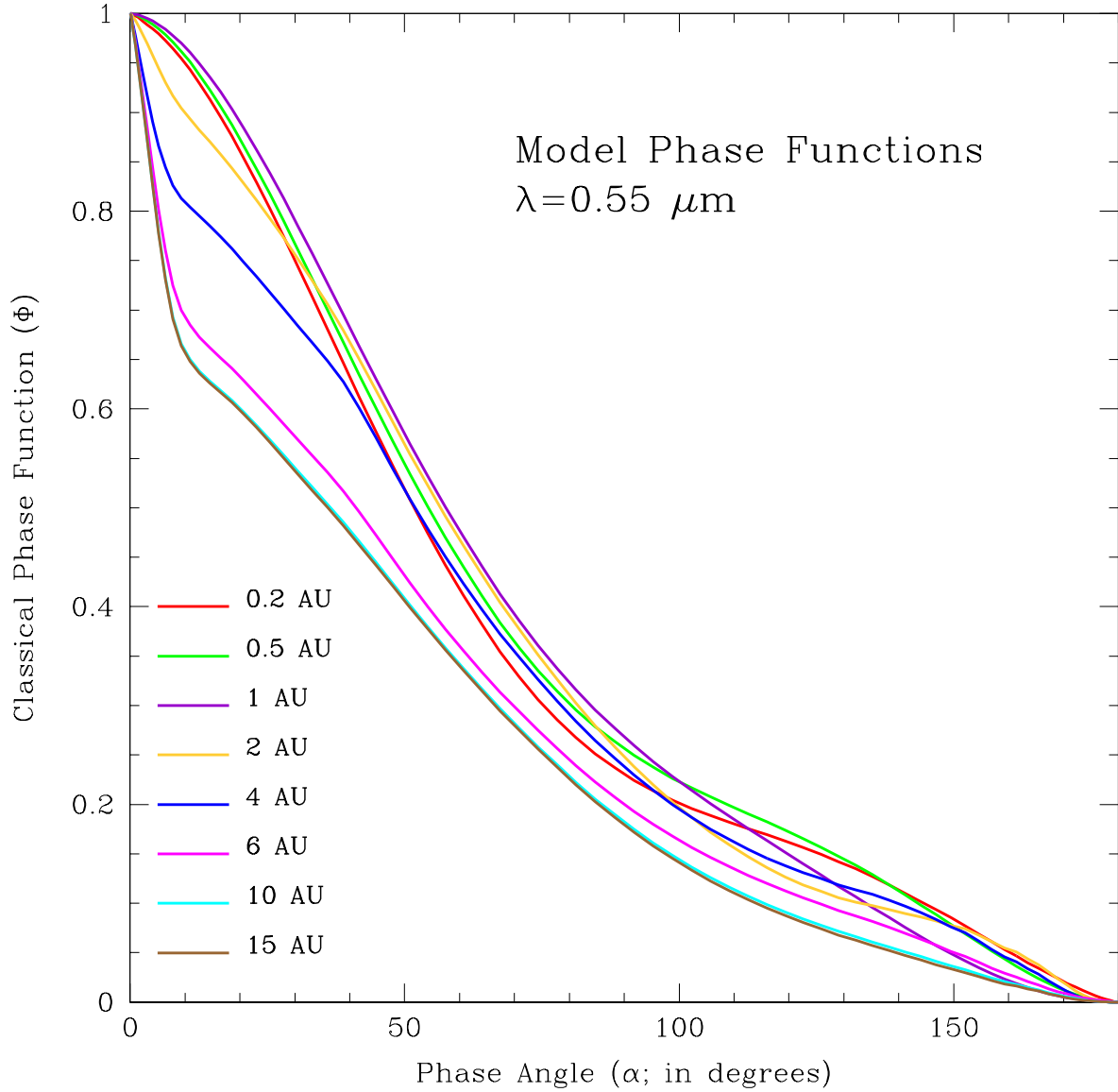


Fig. 5.— Theoretical optical phase functions of $1-M_J$, 5-Gyr EGPs ranging in orbital distance from 0.2 AU to 15 AU from a G2V star. Near full phase, the phase functions for our baseline models at larger orbital distances peak most strongly. For the cloud-free EGPs at smaller orbital distances (0.2 AU, 0.5 AU, and 1 AU), the phase functions are more rounded near full phase.

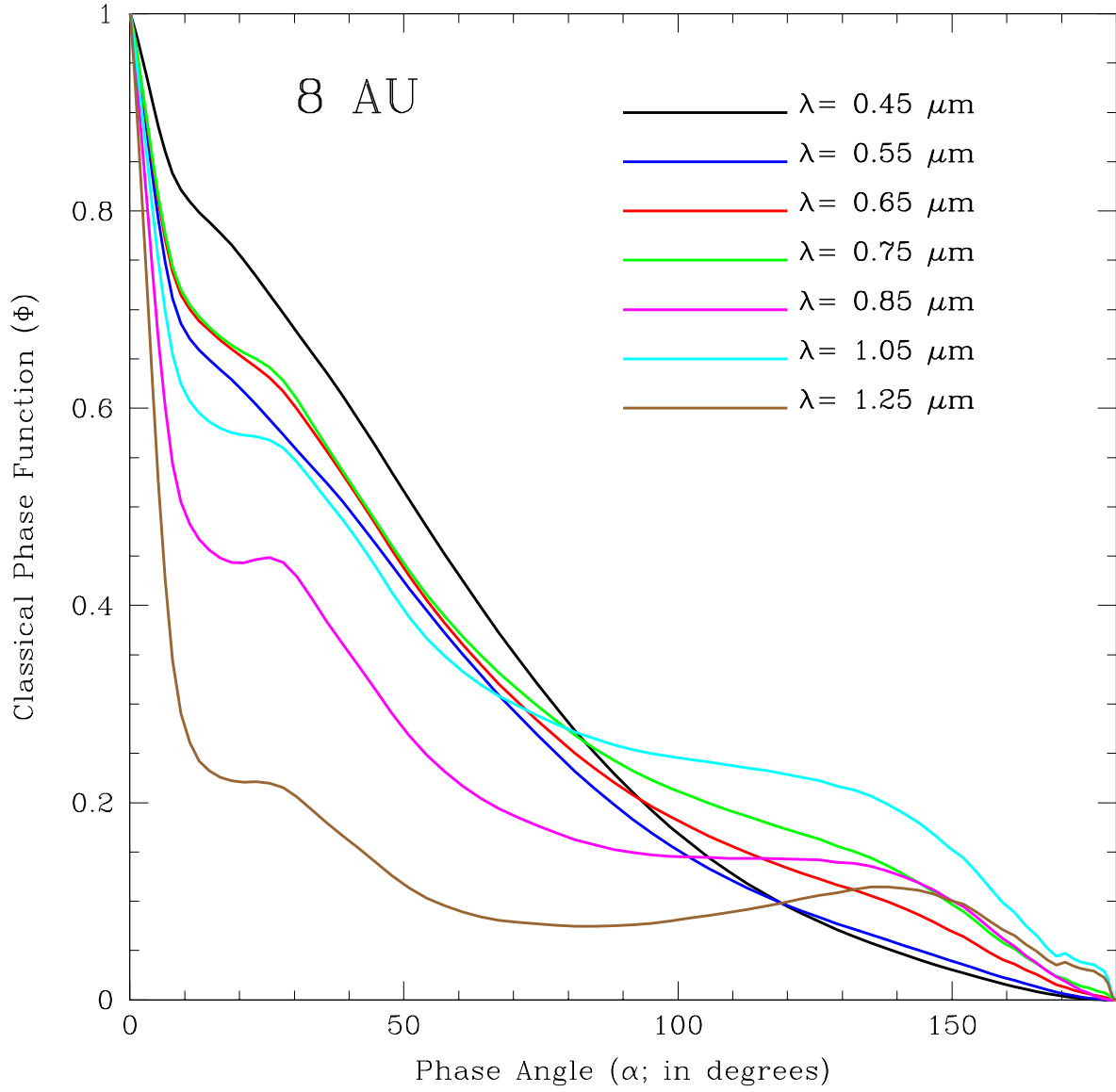


Fig. 6.— Wavelength dependence of the phase function for an EGP orbiting at a distance of 8 AU from its G2V central star. The EGP contains an ammonia cloud layer above a deeper water cloud.

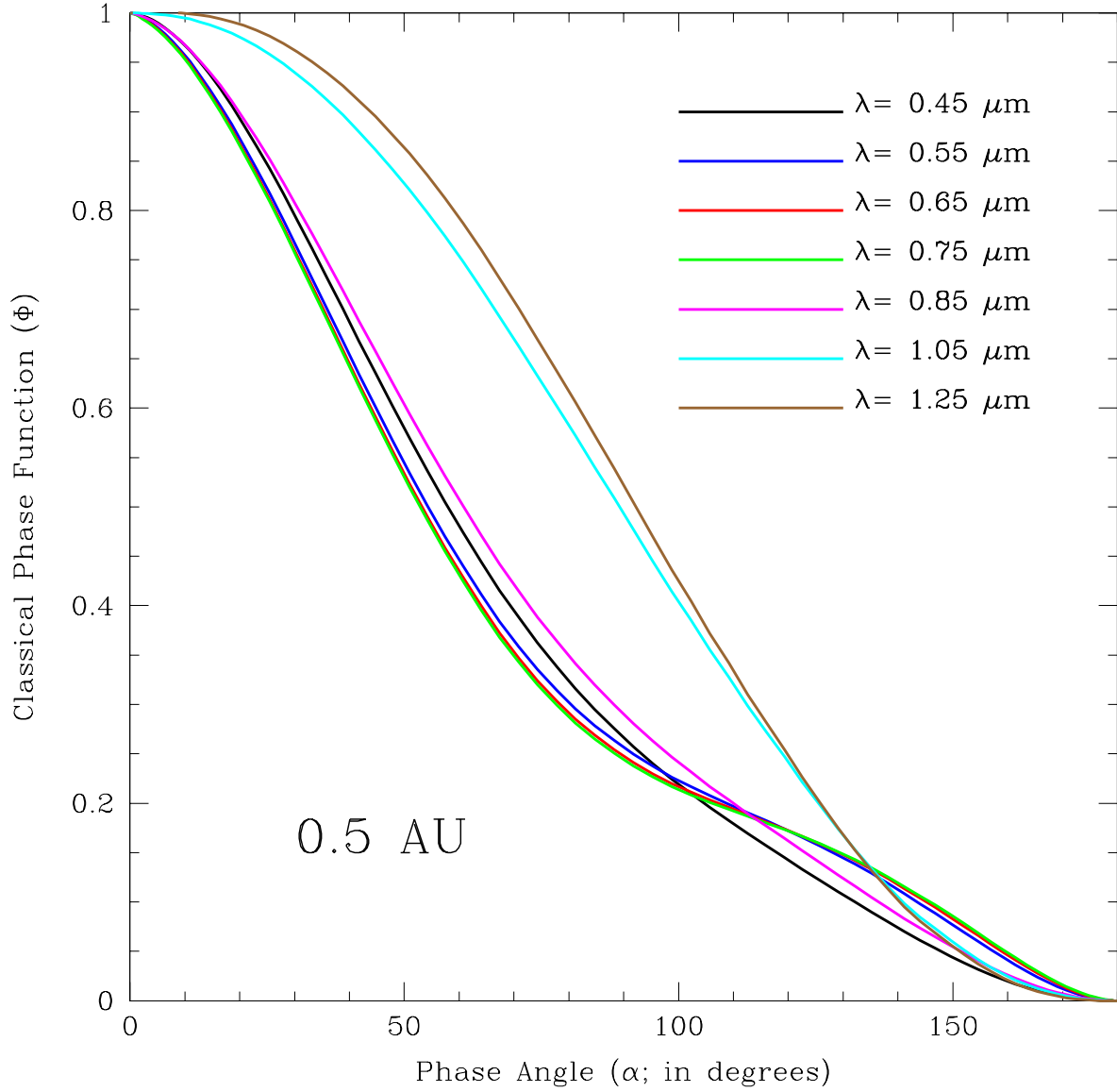


Fig. 7.— Wavelength dependence of the phase function for a cloud-free EGP orbiting at a distance of 0.5 AU from its G2V central star. The $1.05 \mu\text{m}$ and $1.25 \mu\text{m}$ phase curves are outliers because they contain a mix of thermally re-emitted and reflected radiation.

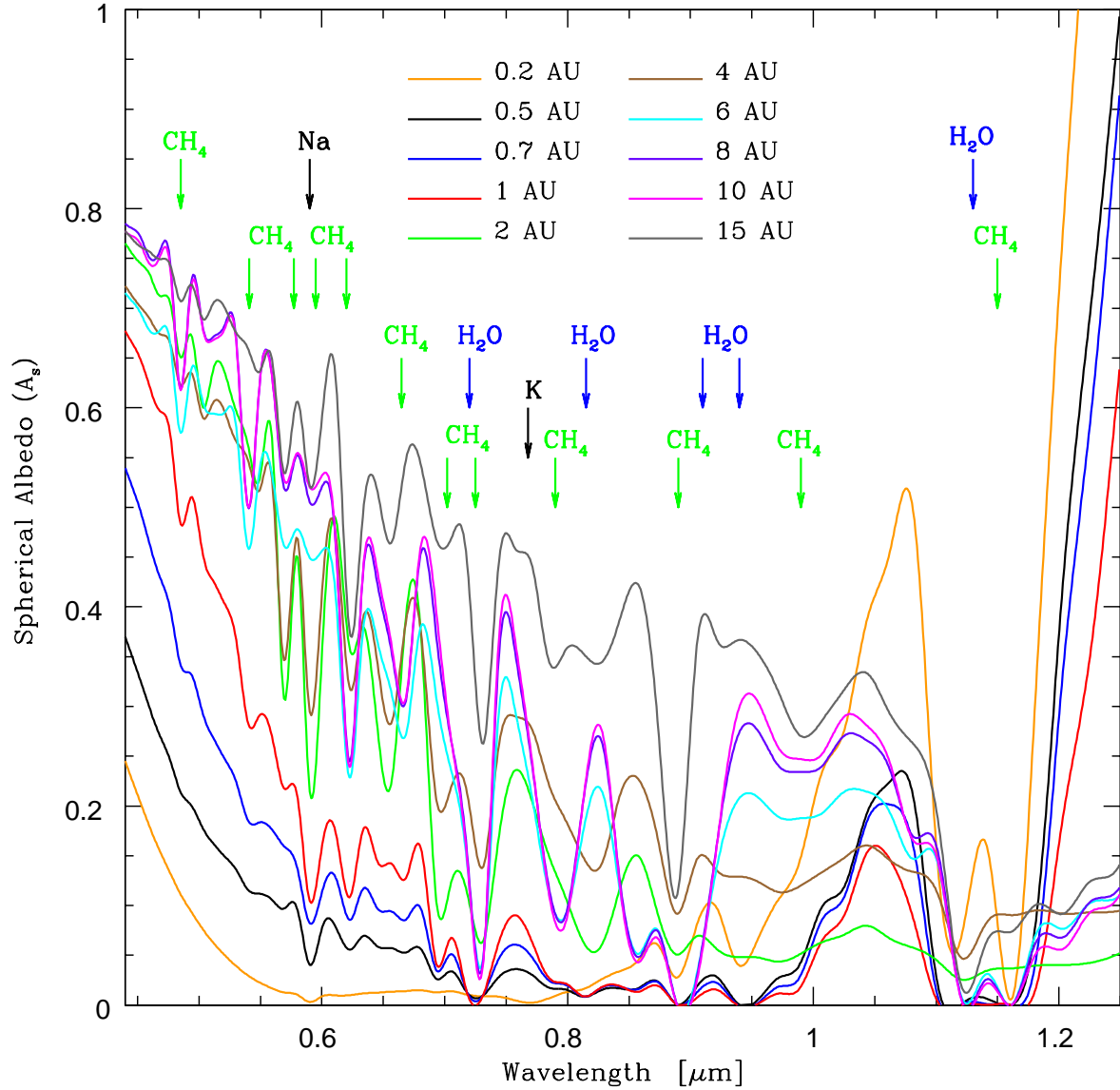


Fig. 8.— Low-resolution, wavelength-dependent spherical albedos of $1-M_J$, 5 Gyr EGPs ranging in orbital distance from 0.2 AU to 15 AU about a G2V star. Cubic splines are fit to all albedo data. The high albedos at short wavelengths are due to Rayleigh and/or condensate scattering (reddening effects of photochemical hazes are not incorporated into these models). At wavelengths longer than $\sim 1 \mu\text{m}$, the high “albedo” values shown are due mainly to thermal re-emission, not reflection.

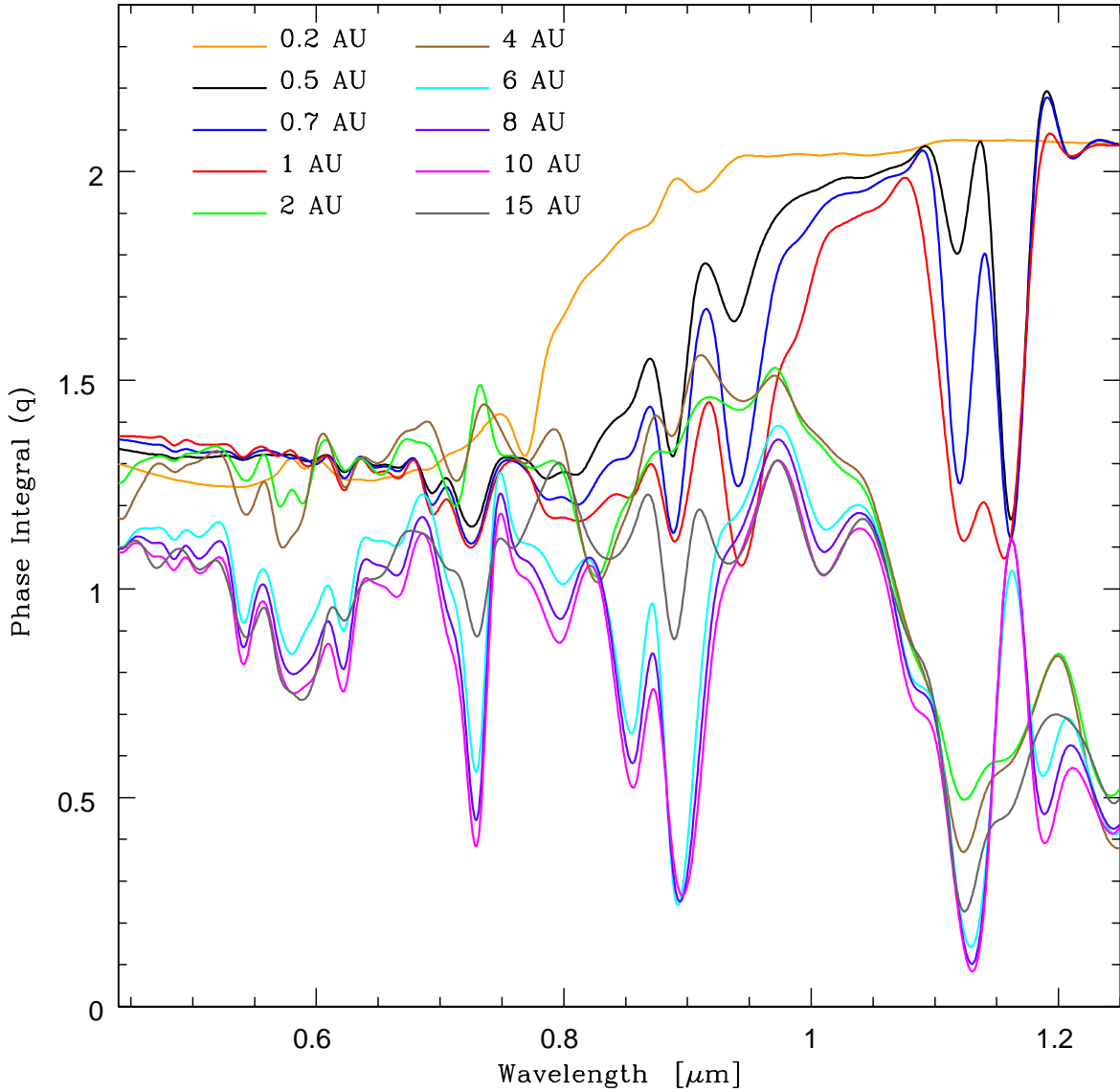


Fig. 9.— Low-resolution, wavelength-dependent phase integrals of $1-M_J$, 5 Gyr EGPs ranging in orbital distance from 0.2 AU to 15 AU about a G2V star. Cubic spline curves are fit to the data. Due to backscattering effects, cloudy models, particularly those with ammonia clouds, tend to have smaller phase integrals.

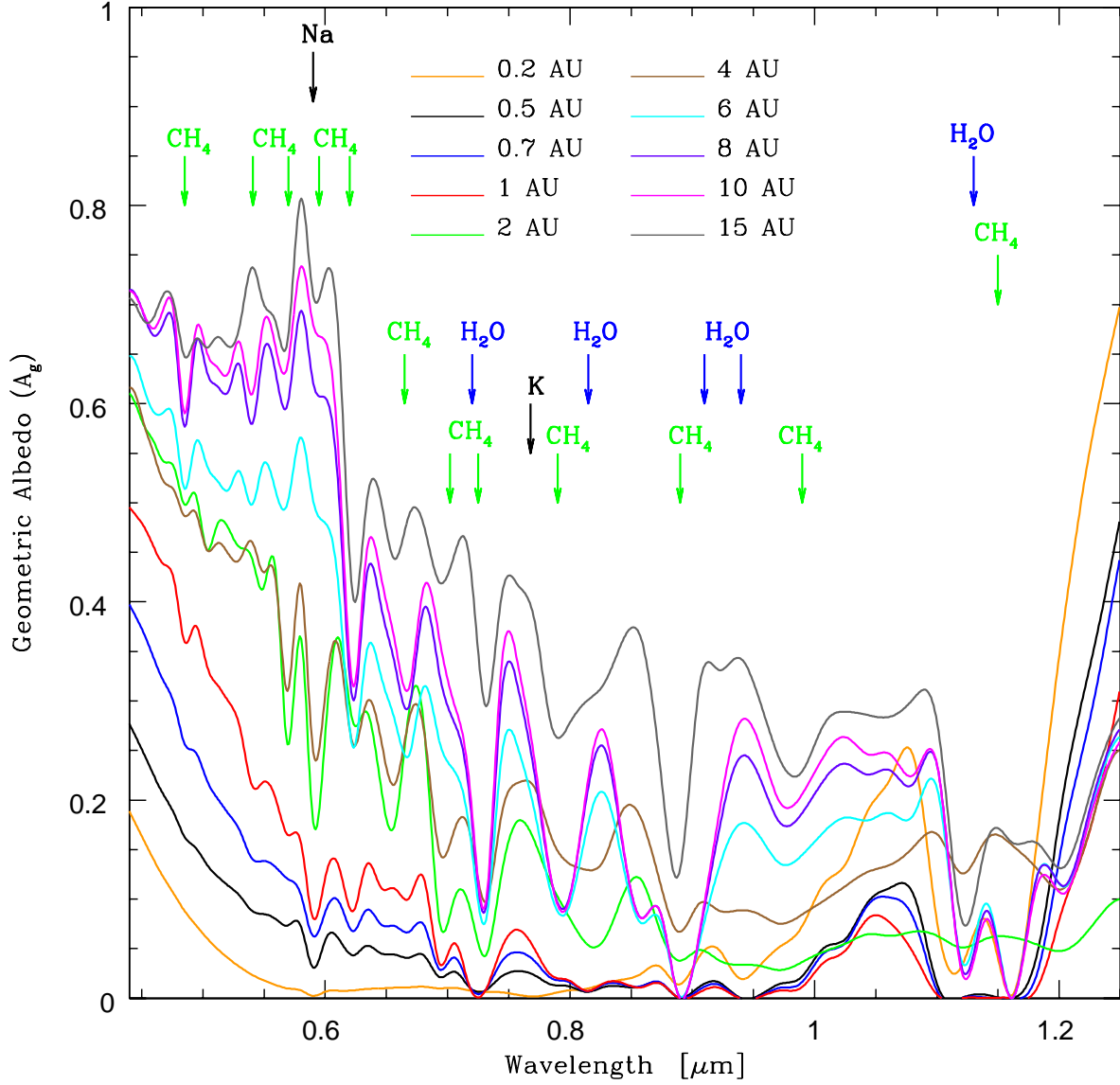


Fig. 10.— Low-resolution, wavelength-dependent geometric albedos of $1-M_J$, 5 Gyr EGPs ranging in orbital distance from 0.2 AU to 15 AU about a G2V star. Cubic splines are fit to all albedo data. As in Fig. 8, reddening effects of photochemical hazes are not incorporated.

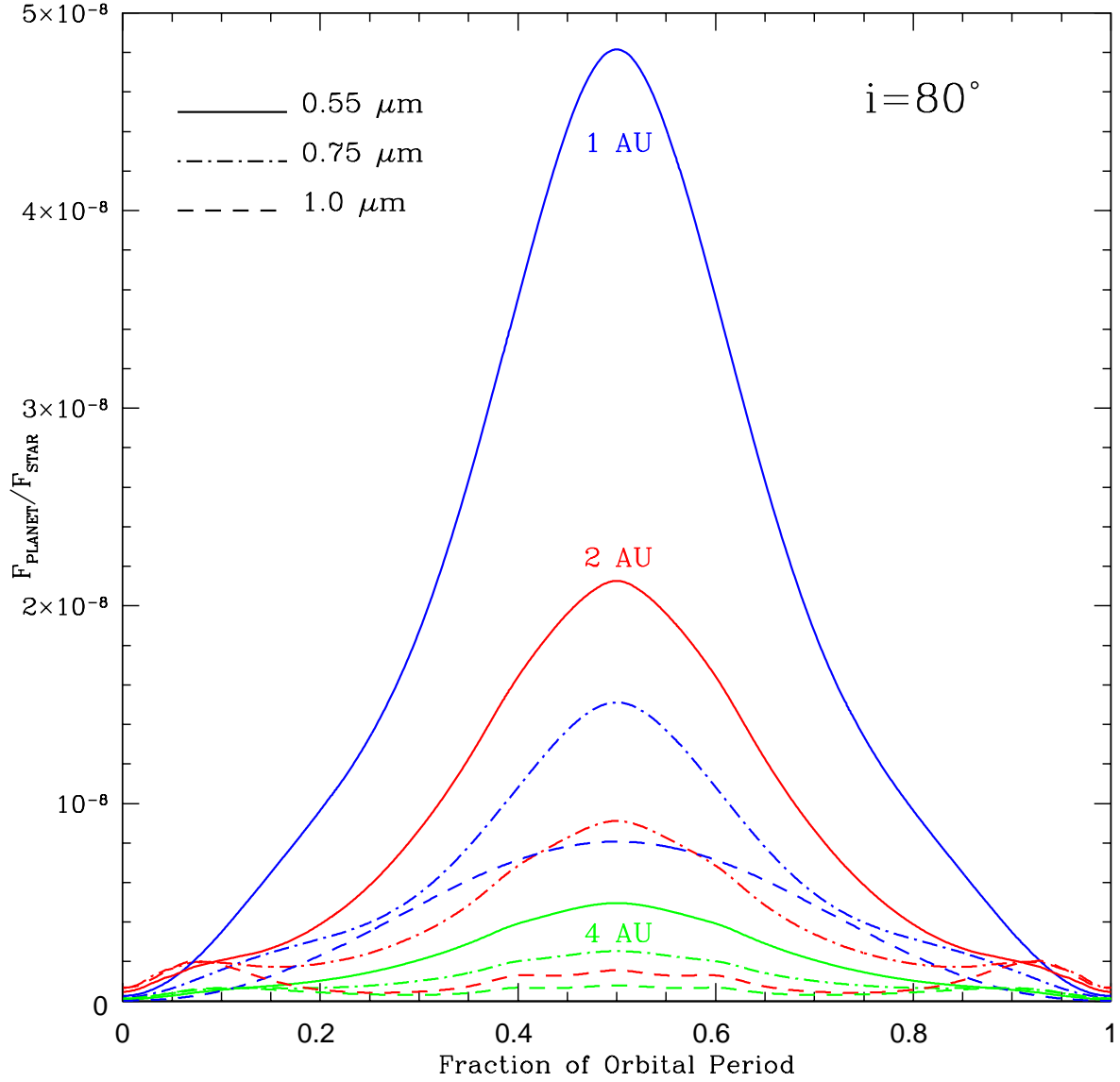


Fig. 11.— Light curves at $0.55 \mu\text{m}$, $0.75 \mu\text{m}$, and $1 \mu\text{m}$ for our model EGPs in circular orbits inclined to 80° at distances of 1 AU, 2 AU, and 4 AU from a G2V star. The models at 2 AU and 4 AU contain water ice clouds in their upper atmospheres, while the 1 AU model does not.

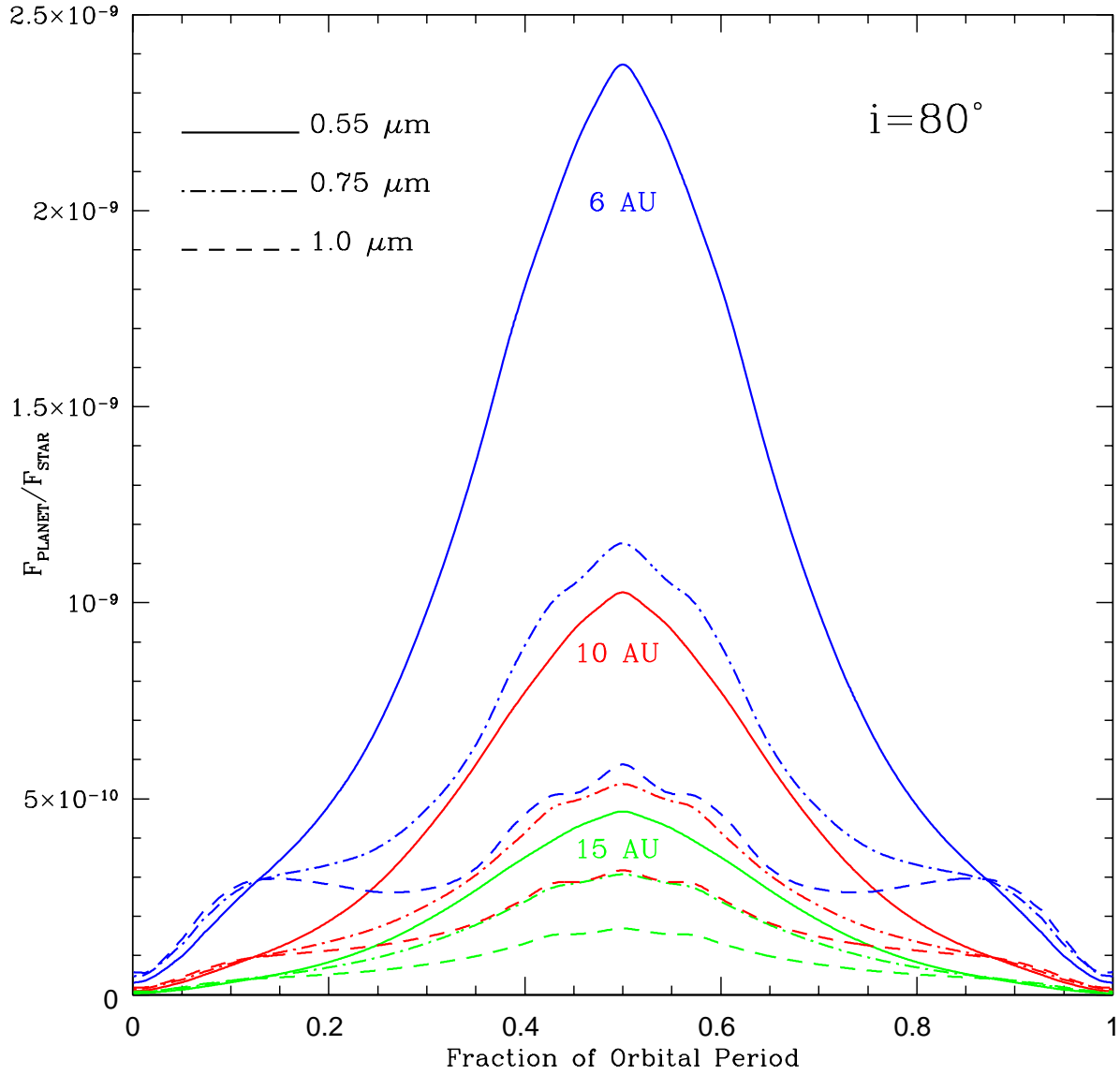


Fig. 12.— Light curves at 0.55 μm , 0.75 μm , and 1 μm for our model EGPs in circular orbits inclined to 80° at distances of 6 AU, 10 AU, and 15 AU from a G2V star. Each of these models contains an ammonia ice cloud layer above a deeper water cloud deck.

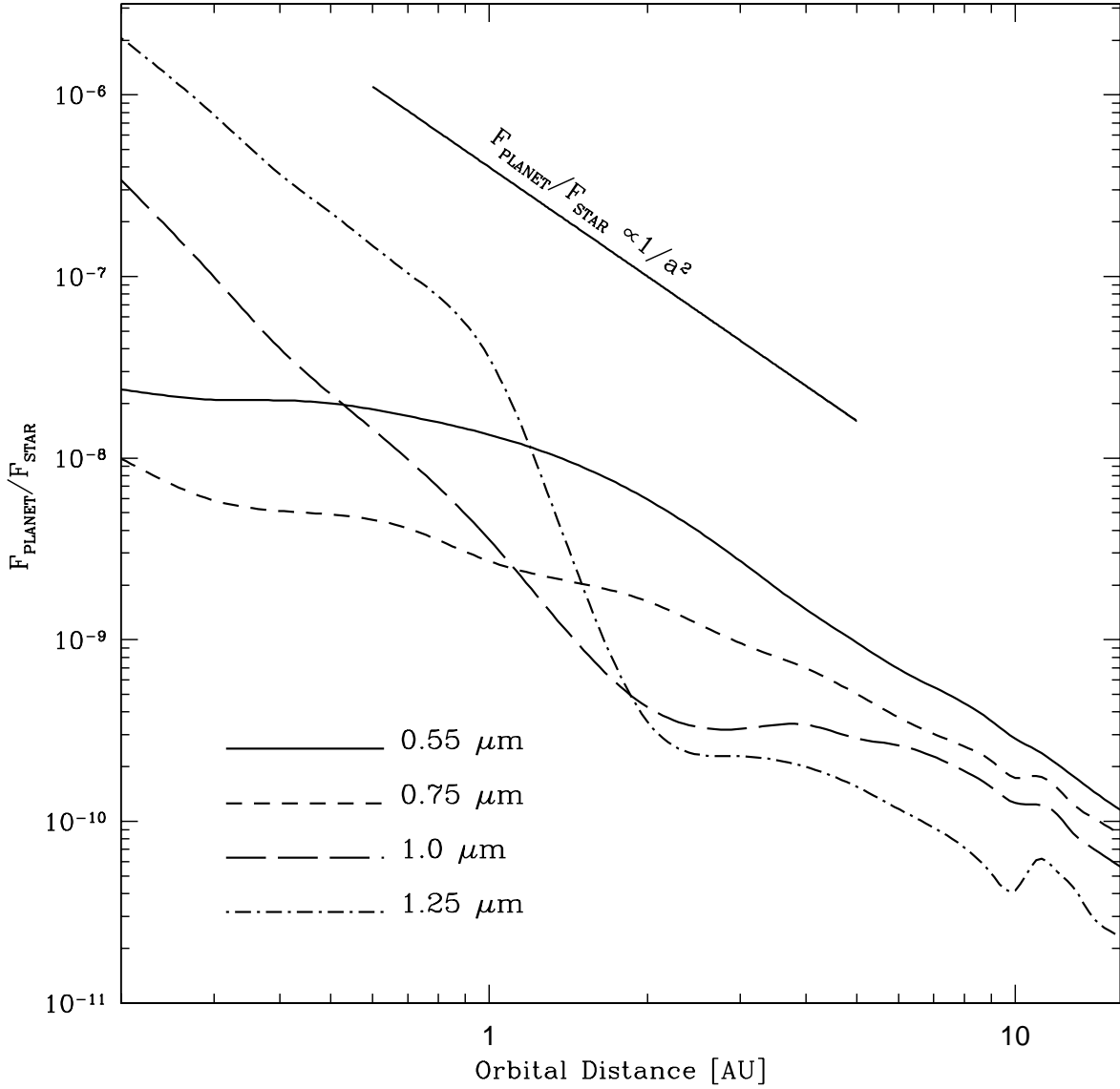


Fig. 13.— Planet/star flux ratio as a function of orbital distance at 0.55 μm , 0.75 μm , 1 μm , and 1.25 μm assuming a G2V central star. In each case, the plotted value corresponds to a planet at greatest elongation with an orbital inclination of 80° . Note that the planet/star flux ratios do not follow a simple $1/a^2$ law.

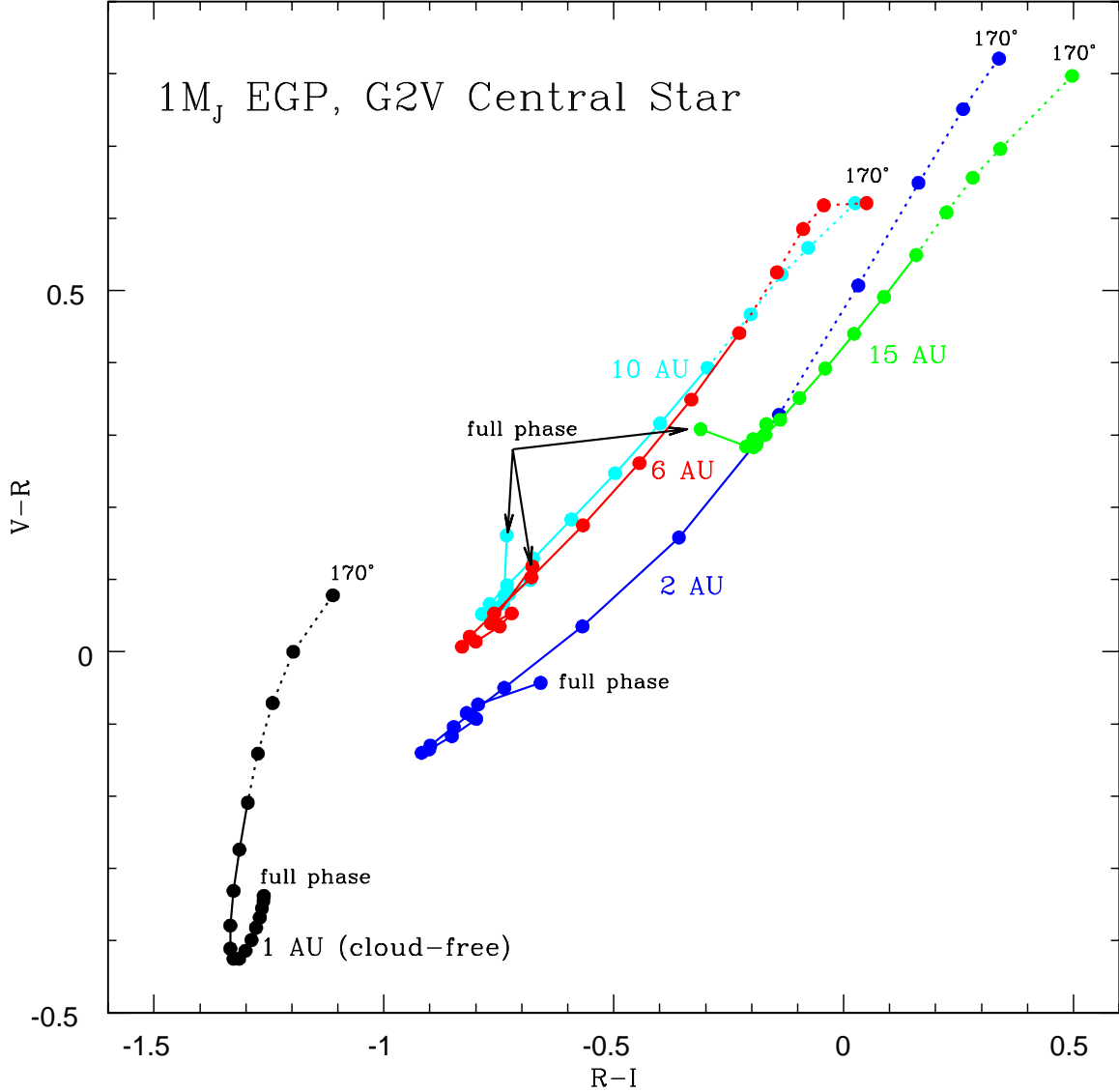


Fig. 14.— $V - R$ vs. $R - I$ color-color diagram detailing variations with planetary phase for a variety of orbital distances. Each of the curves depicts an orbit from full phase (0°) to a thin crescent phase (170°) in increments of 10° (as indicated by the filled circles). Cloud-free EGPs are bluest near greatest elongation, while cloudy EGPs tend to be bluest in a gibbous phase. As full phase is approached, the colors redden somewhat. However, the crescent phases appear to be far redder, varying by as much as a full astronomical magnitude from their blue gibbous-phase colors in some cases. See text for details and a discussion of the accuracy at large phase angles (denoted by dotted lines).

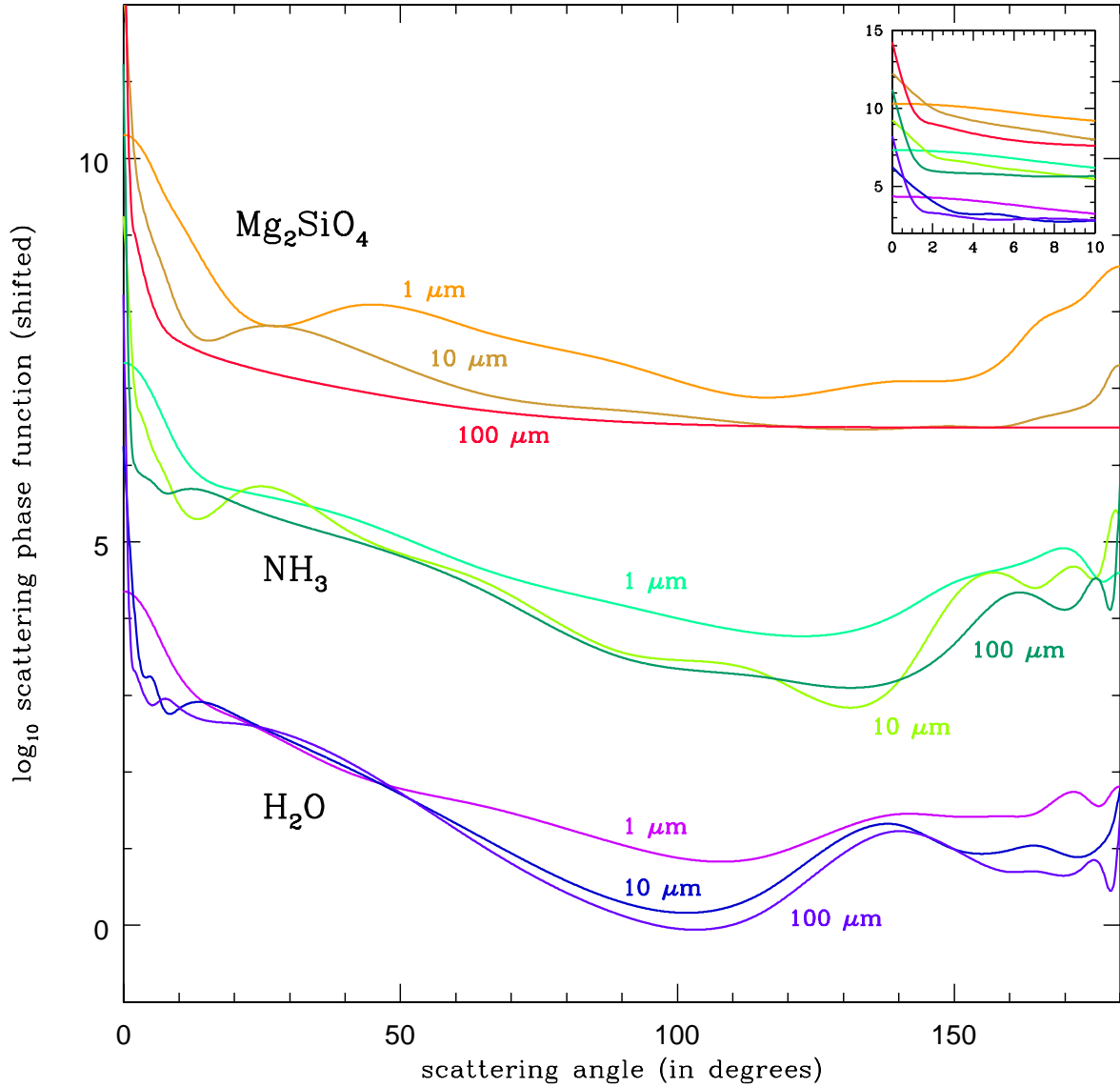


Fig. 15.— Mie theory optical angular scattering dependence of H_2O ice, NH_3 ice, and forsterite grains at modal particle sizes of $1\ \mu\text{m}$, $10\ \mu\text{m}$, and $100\ \mu\text{m}$ on a logarithmic scale. A Deirmendjian particle size distribution is assumed. Each scattering phase function is normalized to the $1\text{-}\mu\text{m}$ particle size (for easy comparison) and fit with a cubic spline. Furthermore, the various species are offset for readability, so the phase function values are dimensionless. The inset figure, also on a logarithmic scale, shows the degree of forward peaking at small phase angles.

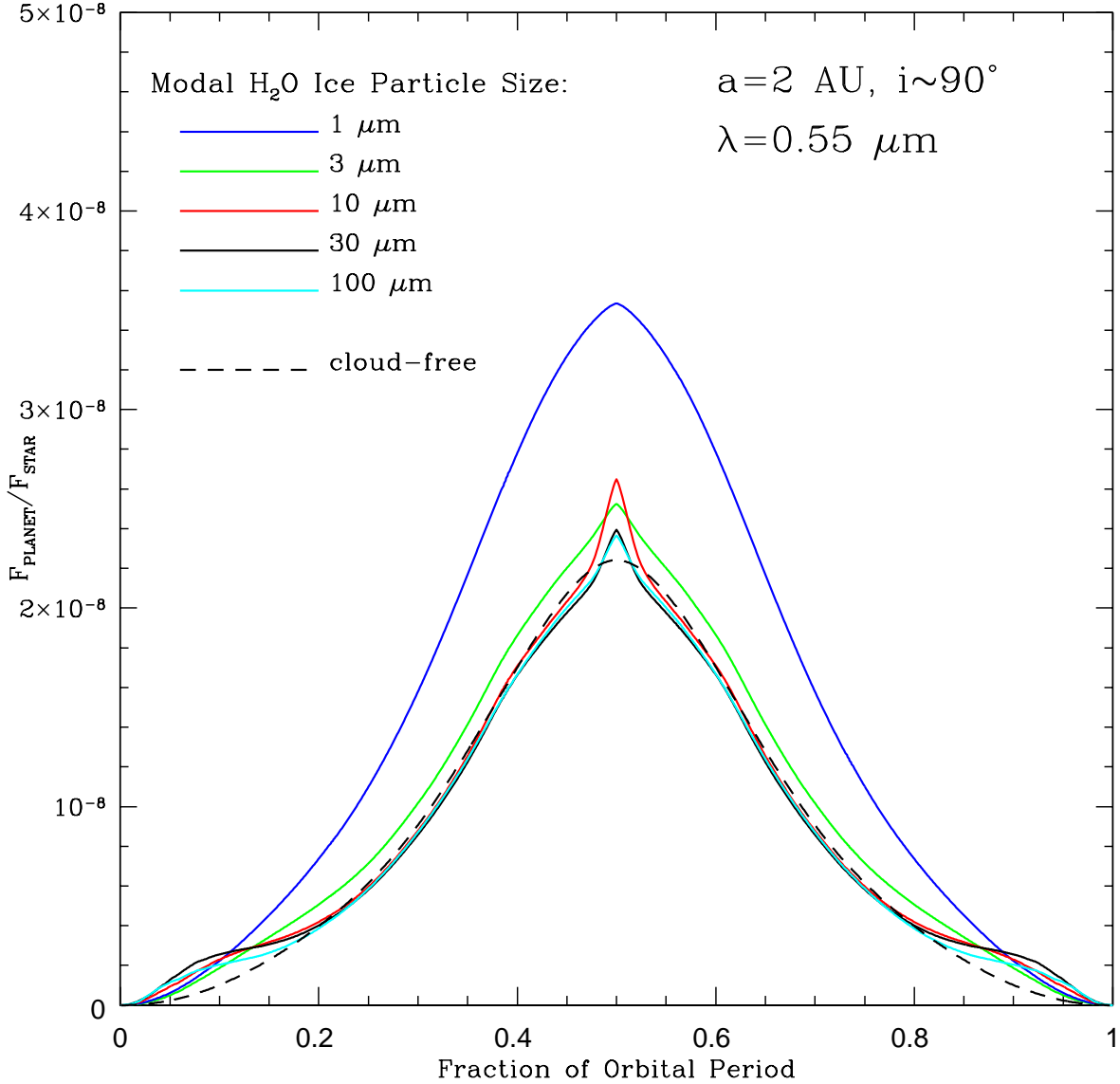


Fig. 16.— The dependence of the planet/star flux ratio on condensate particle size at a wavelength of $0.55 \mu\text{m}$. Model light curves for EGPs at 2 AU with modal H₂O ice particle sizes of 1, 3, 10, 30, and 100 μm are depicted. Shown for comparison is a cloud-free model (*black dashed curve*). In order to show the full variation in the shapes and magnitudes of the light curves with particle size, we have set the orbital inclination to $\sim 90^\circ$ so that the opposition effect, present for many of the models, can be seen in full. Transit effects are not modeled.

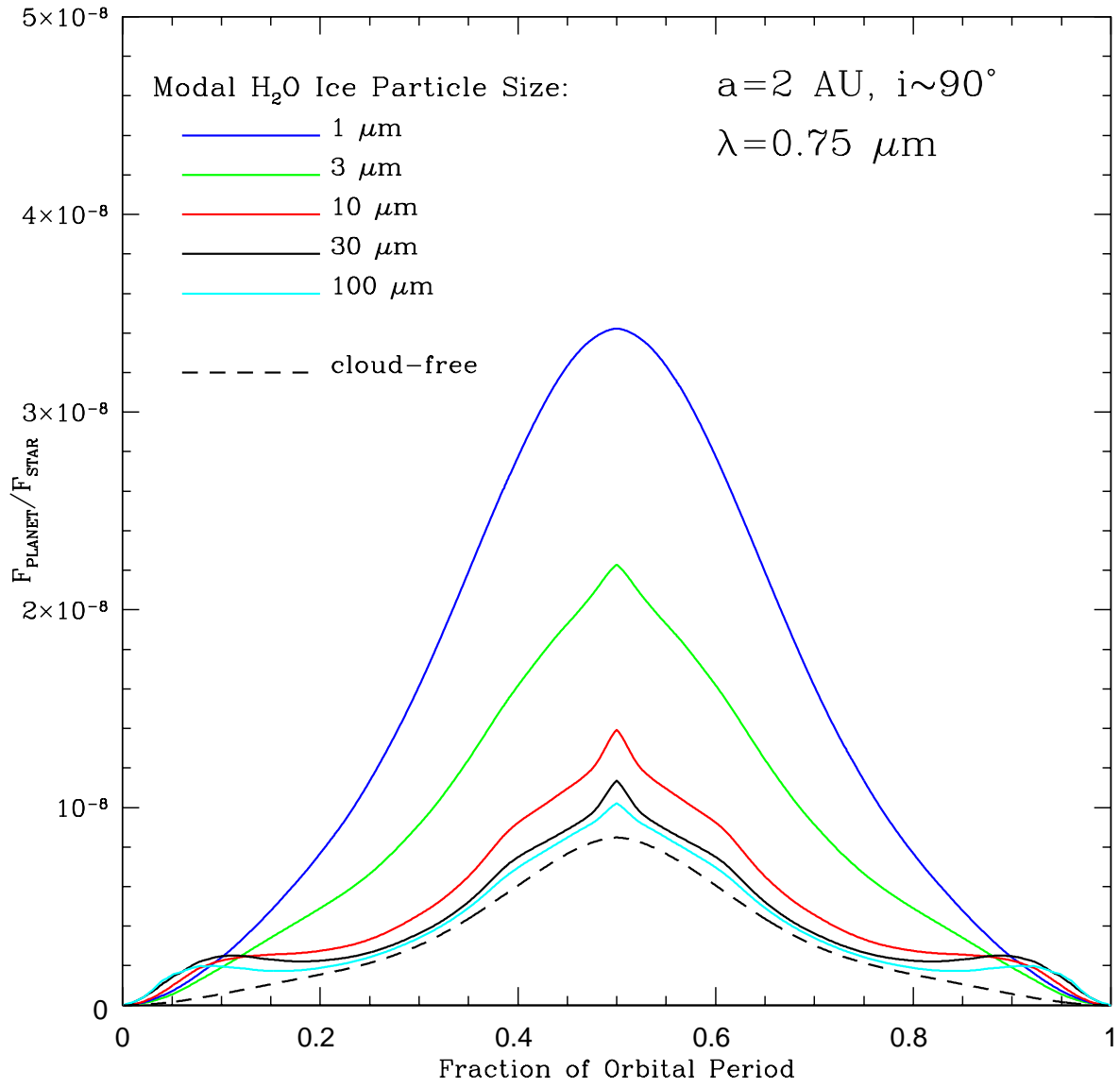


Fig. 17.— Same as Fig. 16, except at 0.75 μm.

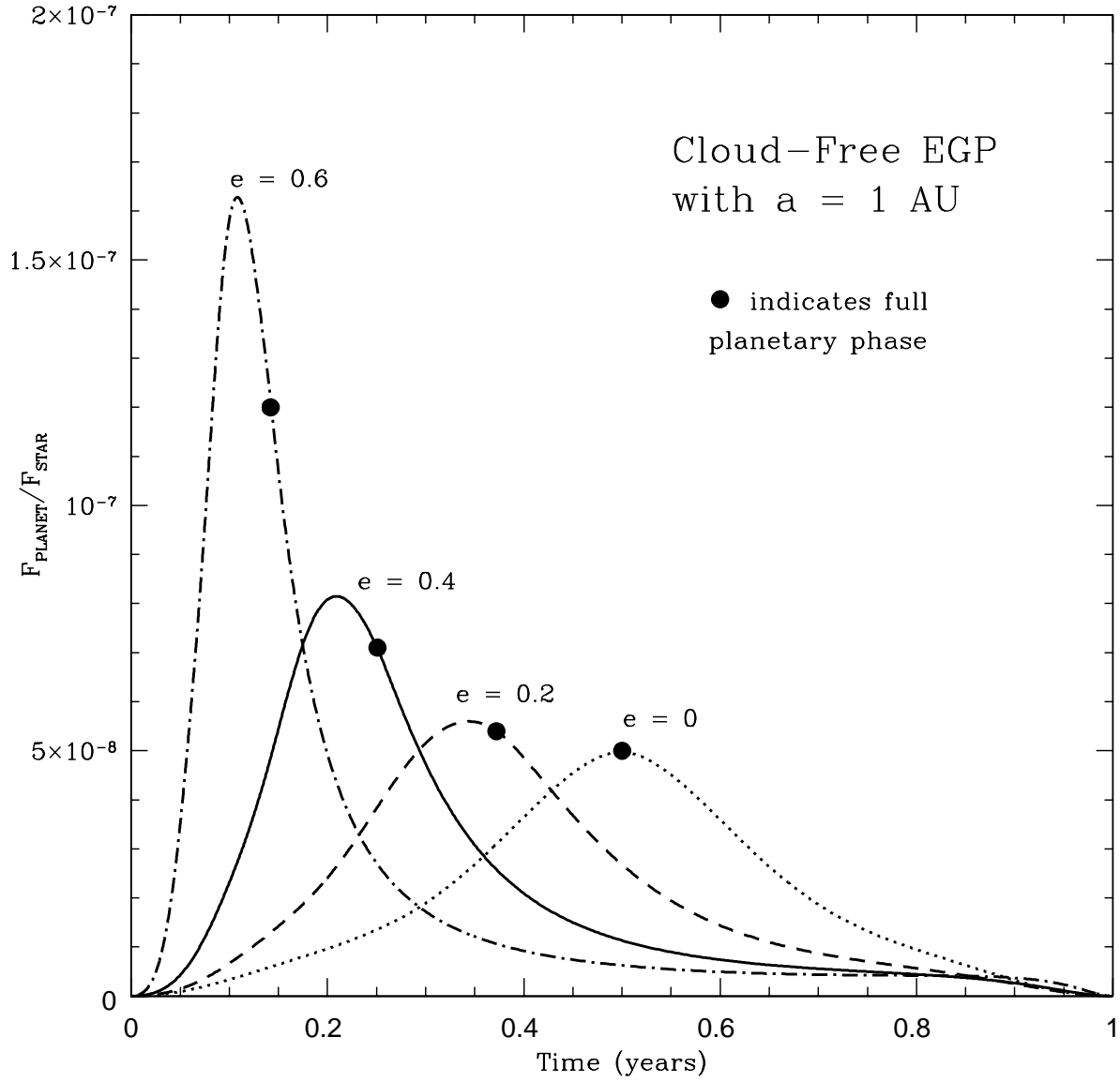


Fig. 18.— The optical planet/star flux ratio as a function of eccentricity for a cloud-free EGP at 1 AU, fixing Ω and i at 90° and ω at 0° (see text for details). Only for $e=0$ does the peak of the light curve coincide with full phase.

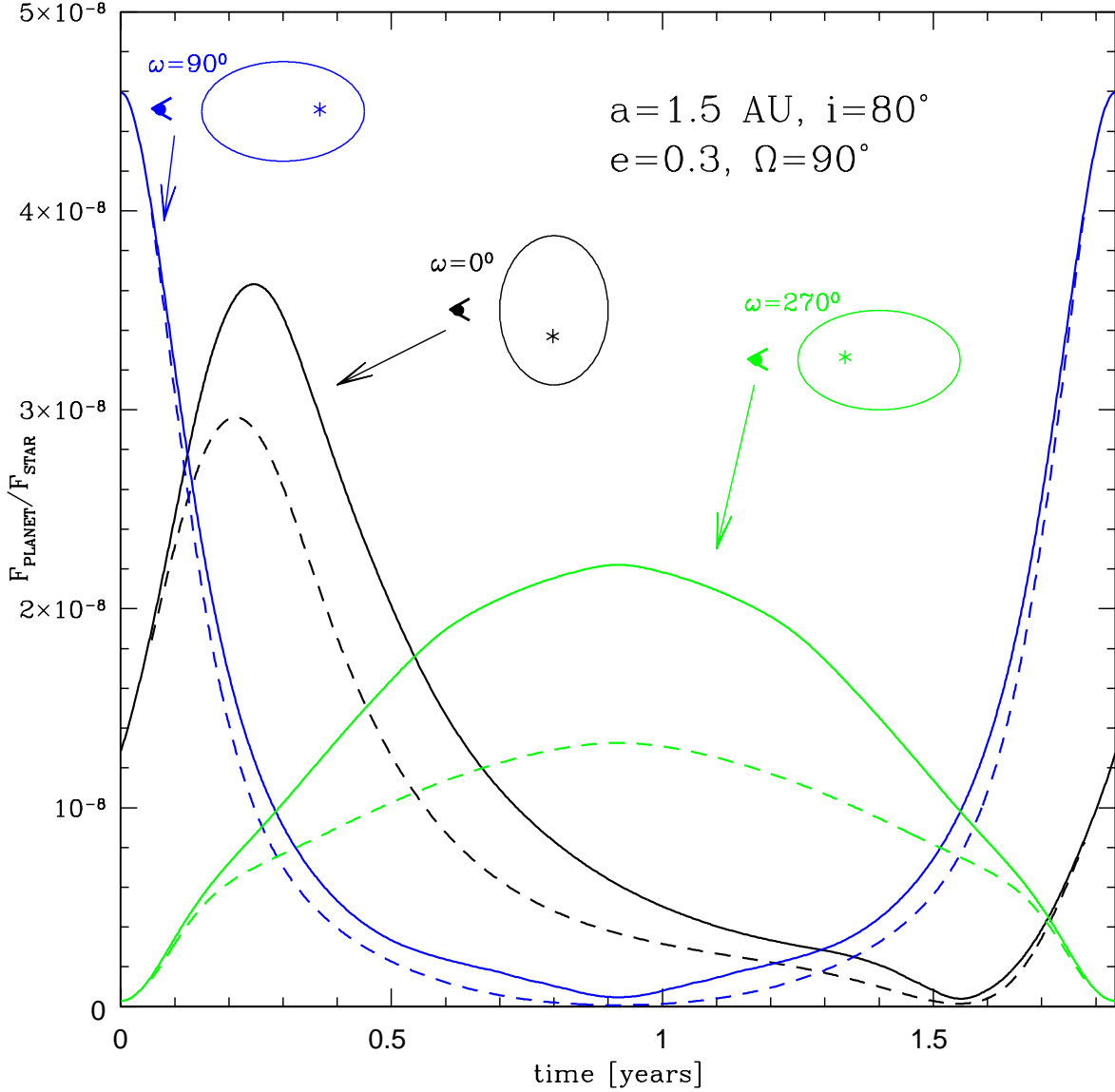


Fig. 19.— The optical light curve of an EGP with $a=1.5 \text{ AU}$ and $e=0.3$, assuming a G2V central star (a system similar to HD 160691; Jones *et al.* 2002) and an inclination of 80° (with no transit effects). Three different possible viewing angles are shown (*solid curves*). Clouds condense and sublimate throughout each orbit as the planet-star distance varies in time. Shown for the sake of comparison are the light curves that would result if the object were to remain artificially cloud-free throughout its entire orbit (*dashed curves*).

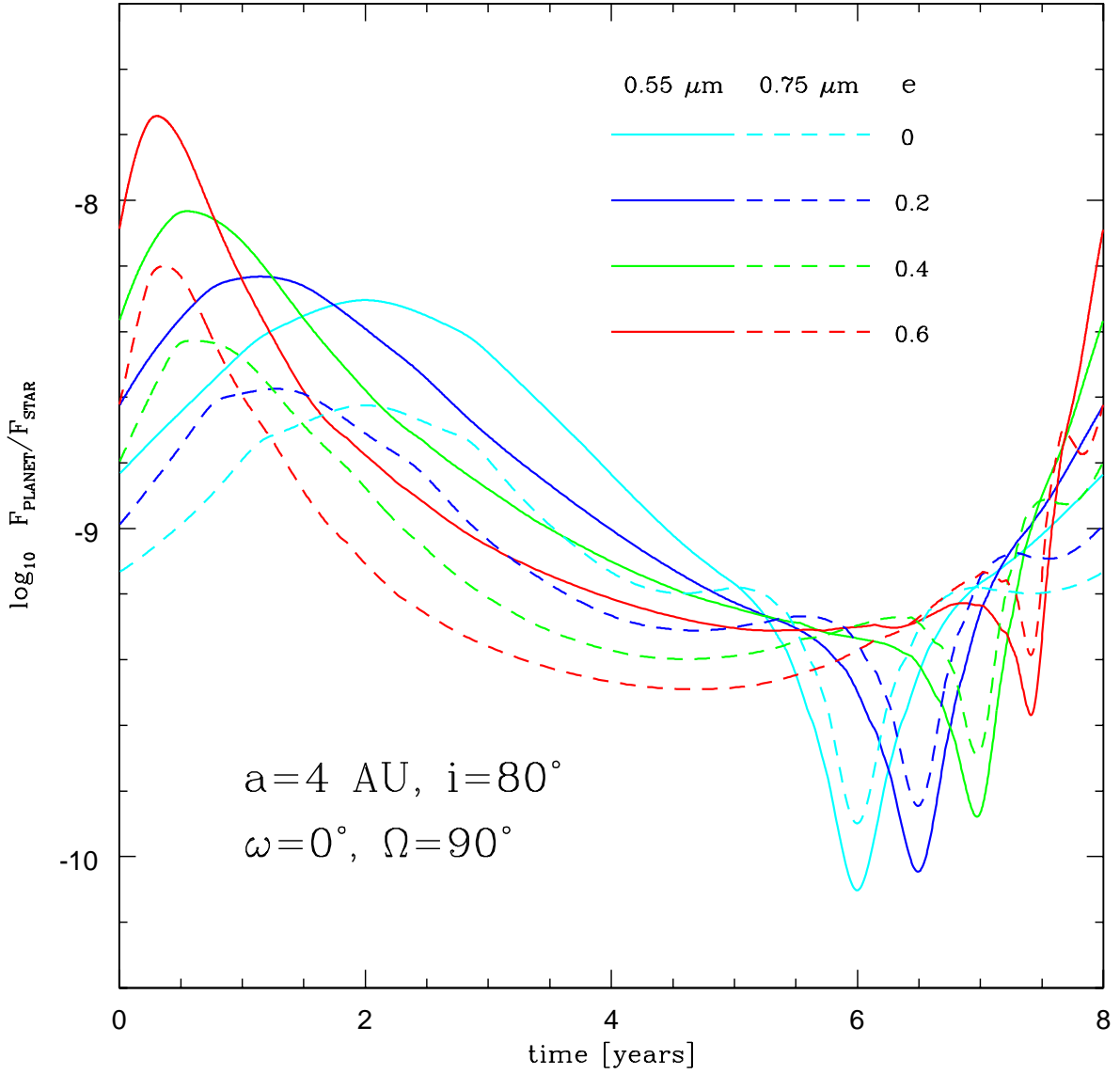


Fig. 20.— The logarithm of the optical (at $0.55 \mu\text{m}$) and far red ($0.75 \mu\text{m}$) planet/star flux ratios as a function of eccentricity for $a = 4 \text{ AU}$, fixing i at 80° , Ω at 90° and ω at 0° . The planet/star flux ratio is a factor of 2 to 3 greater at $0.55 \mu\text{m}$ than in the far red at most planetary phases.

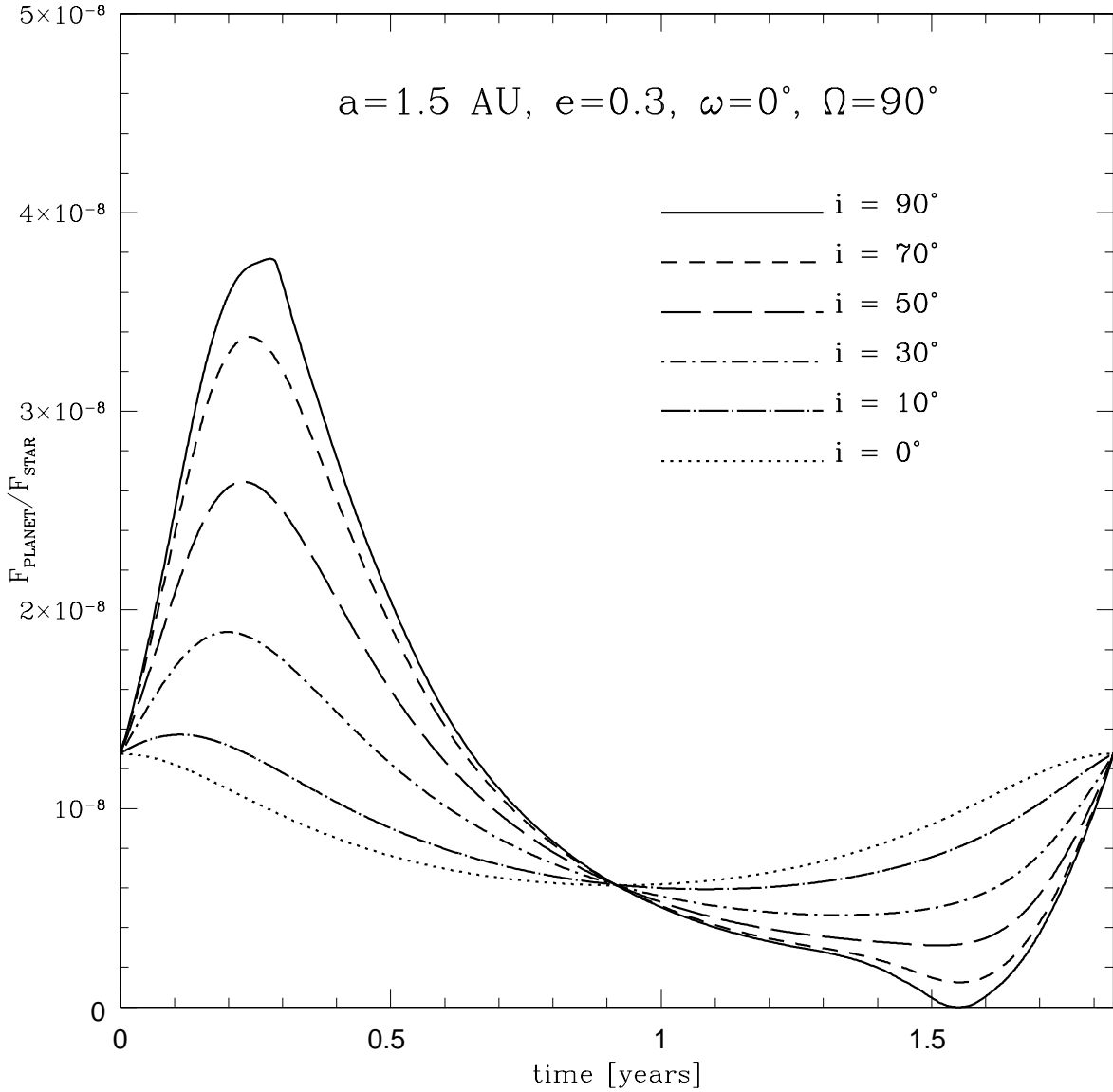


Fig. 21.— Variation with inclination of the optical light curve for an elliptical orbit (G2V central star, $a = 1.5 \text{ AU}$, $e = 0.3$). For a highly-inclined orbit, the peak of the planet/star flux ratio is a factor of ~ 3 greater than for a face-on ($i = 0^\circ$) orbit. The (symmetric) variation for the face-on case is due entirely to the variation in the planet-star distance over an eccentric orbit.

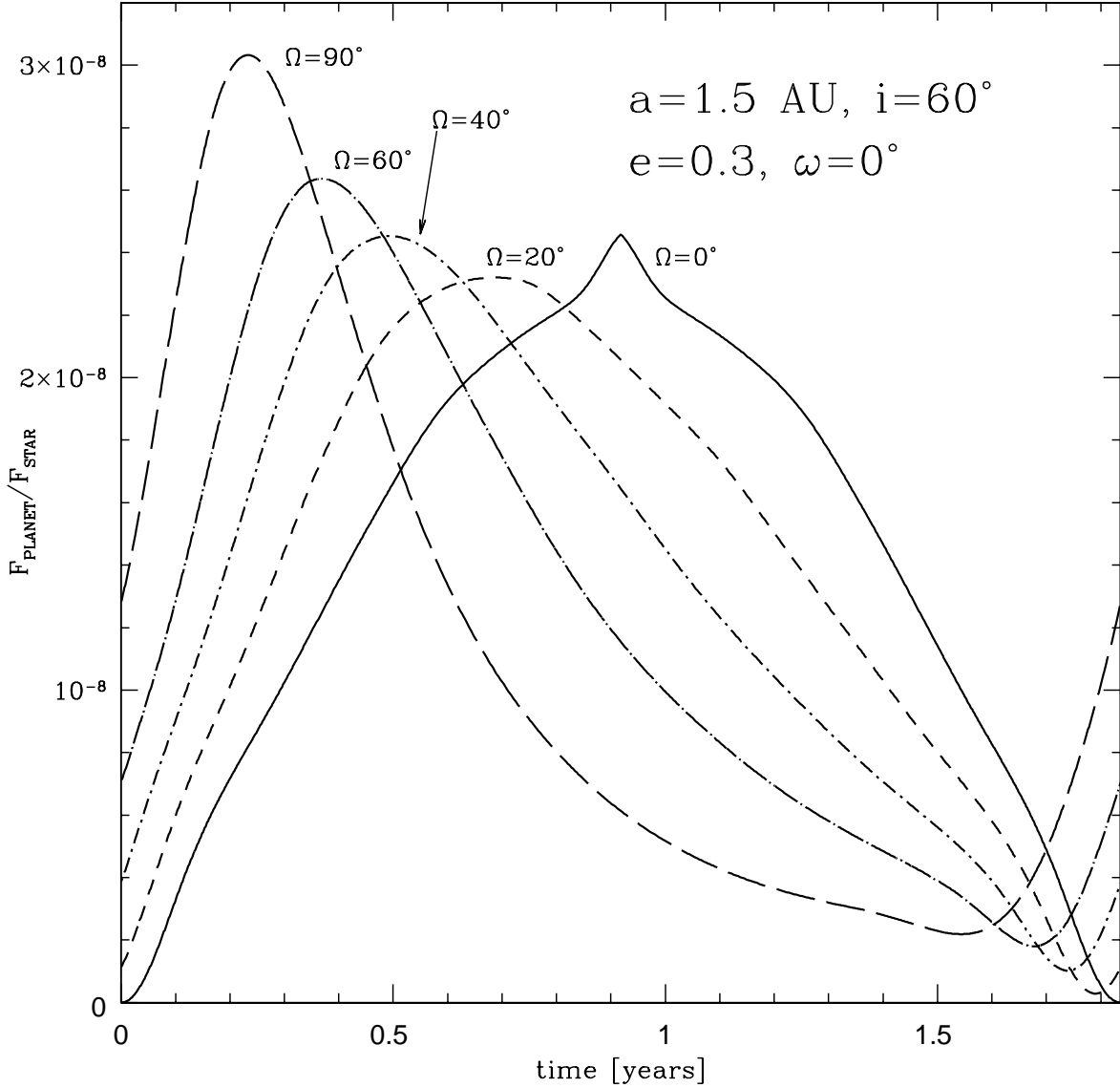


Fig. 22.— Variation with the longitude of the ascending node (Ω) of the optical light curve for an elliptical orbit, assuming $a = 1.5 \text{ AU}$, $e = 0.3$, $i = 60^\circ$, and $\omega = 0^\circ$. The peak of the light curve shifts from ~ 0.25 years for $\Omega = 90^\circ$ to ~ 0.9 years (half the orbital period) for $\Omega = 0^\circ$. The peak for $\Omega = 0^\circ$ is the full-phase opposition effect.